frontiers | Frontiers in Earth Science

TYPE Original Research
PUBLISHED 10 December 2024
DOI 10.3389/feart.2024.1508394

Petrogenesis of the paleoproterozoic ultramafites in Wuchuan area, Inner Mongolia: implications for tectonic evolution

Hao Hu, Dongyan Zhong, Zhiguang Zhou*, Guosheng Wang, Shen Gao, Jianfeng Chen and Chenfei Feng

School of Earth Sciences and Resources, China University of Geosciences Beijing, Beijing, China

Check for updates

OPEN ACCESS

EDITED BY
Chen Zhao,
Shenyang Center of China Geological Survey, China

REVIEWED BY
Wang Xiao,
The University of Hong Kong, Hong Kong SAR, China
Bin Wu,
Northwest University, China

*CORRESPONDENCE
Zhiguang Zhou,
zhouzhg@cugb.edu.cn

RECEIVED 09 October 2024
ACCEPTED 26 November 2024
PUBLISHED 10 December 2024

CITATION
Hu H, Zhong D, Zhou Z, Wang G, Gao S, Chen J and Feng C (2024) Petrogenesis of the paleoproterozoic ultramafites in Wuchuan area, Inner Mongolia: implications for tectonic evolution.
Front. Earth Sci. 12:1508394.
doi: 10.3389/feart.2024.1508394

Introduction: The east-west trending Khondalite Belt, located on the northern margin of the North China Craton, is linked to the Paleoproterozoic Columbia supercontinent's evolution. However, the relationship between the Khondalite Belt formation and orogenic processes remains unclear.

Methods: Field investigations, petrology, zircon U-Pb dating, whole-rock geochemistry, and electron probe mineral thermobarometry.

Results: Garnet-bearing pyroxenite and serpentinite-like dunite in the ultramafites have zircon U-Pb ages of (1947 $\pm$ 17) Ma and (1960 $\pm$ 25) Ma, respectively. The rocks show characteristics of subalkaline tholeiitic basalt series, with low SiO_2 (35.79%–50.77%), TiO2 (0.01%–0.71%), Al_2O_3 (0.17%–3.39%), and alkalis (0.02%–2.01%), but high Fe_2O_3 (12.92%–15.06%). These rocks are enriched in light rare earth elements with slight depletion of Eu, enriched in large ion lithophile elements (Rb and K), and depleted in high field strength elements (P, Zr, and Hf).

Discussion: These metamorphic environments imply that the conditions for ultramafites formation were insufficient to induce granulite-facies metamorphism in the surrounding rocks, indicating that granulite-facies metamorphism in the Khondalite Belt is not closely related to post-orogenic extension in the Inner Mongolia-Northern Hebei orogenic belt.

KEYWORDS

ultramafites, Inner Mongolia-North Hebei orogenic belt, Khondalites, zircon U-Pb geochronology, geochemistry

1 Introduction

The concept of the "supercontinent cycle" has been crucial in solid Earth sciences since its inception, focusing primarily on the processes of supercontinent assembly and breakup (Nance et al., 1988; Taylor and McLennan, 1995; Li and Zhong, 2009; Nance, 2022). Supercontinents assemble primarily through global-scale accretion and collisional orogeny (Murphy and Nance, 2013; Li, 2021). Recent studies indicate that the North China Craton collided with other cratons during 2.2–1.85 Ga (Kusky et al., 2016) or the southwestern margin of the Siberian Craton as part of the Columbia supercontinent convergence (Wan B. et al., 2015; Wu et al., 2018; Wu et al., 2022; Wu et al., 2023). These processes formed a significant Paleoproterozoic collisional orogenic belt (Inner Mongolia-Jibei Orogenic Belt) along its northern margin (Kusky and Li, 2003; Kusky and Santosh, 2009; Kusky and Traore, 2023). This belt comprises primarily the Yinshan Block (Kusky et al., 2007a; Kusky et al., 2016) and the Khondalite Belt on the northern margin of the North China Craton (Condie et al., 1992; Kusky and Li, 2003; Kusky, 2011) (Figure 1A). The Khondalite Belt on the northern margin of the North China Craton consists of pelitic/felsic granulite, quartzite, calc-silicate rock, and marble (Lu and Jin, 1993; Zhai, 2022). It has undergone high-pressure (HP) and medium-pressure (MP) granulite facies metamorphism (Yin et al., 2014; Yin et al., 2015; Cai et al., 2017), as well as ultrahigh-temperature (UHT) granulite facies metamorphism (Santosh et al., 2007a; Guo et al., 2012; Liu et al., 2012; Li and Wei, 2018; Gou et al., 2019; Jiao and Guo, 2020; Wang et al., 2020). The origin of the Paleoproterozoic Khondalite Belt is crucial for understanding orogenic evolution during supercontinent convergence. The origin of 1.93–1.90 Ga UHT granulite facies metamorphism is still debated, including (1) upwelling of asthenospheric mantle post-collision (Yin et al., 2009; Huang et al., 2019; Li et al., 2022); (2) subduction of oceanic ridges (Santosh et al., 2008; Peng et al., 2010; Peng et al., 2012); (3) delamination of the lower crust (Zhai and Santosh, 2011; Zhai et al., 2020); (4) lateral flow of the root or post-orogenic root of the orogenic belt (Jiao and Guo, 2020). The relationship between the Khondalite series and contemporaneous mantle-derived magmatic rocks is crucial to elucidate its origin (Liu et al., 2014; Zhai, 2022).

In Inner Mongolia's Wuchuan area, the Paleoproterozoic ultramafites intruded into the Khondalite series at the intersection of the Yinshan Block and the Khondalite Belt, hosting numerous granulite xenoliths. This offers an opportunity to elucidate the relationship between the Khondalite series and mantle-derived magmatic rocks. This study conducted detailed fieldwork on the Wuchuan ultramafites, investigating the occurrences and contact relationships of the gneisses, ultramafites, and granulite xenoliths. Mineral thermobarometry, isotopic dating, and geochemical analysis were used to clarify the relationship between granulite formation and ultramafites emplacement, providing insights into the granulite-facies metamorphism of the Khondalite series and the tectonic evolution of the Inner Mongolia–Northern Hebei orogenic belt.

2 Geological setting

The North China Craton is surrounded by the Central Asian Orogenic Belt to the north during the Late Paleozoic, the Qinling-Dabie Orogenic Belt to the south during the Mesozoic, the Qilian Orogenic Belt to the west during the Early Paleozoic, and the Sulu and Jiao-Liao-Ji Orogenic Belts to the east (Zhao et al., 2001; Xiao et al., 2015; Chen et al., 2022) (Figure 1). During the Paleoproterozoic, an east-west trending orogenic belt existed along the northern margin of the North China Craton, known as the Inner Mongolia-Jibei Orogenic Belt (Kusky et al., 2016; Kusky and Traore, 2023; Wu et al., 2023). The Inner Mongolia-Jibei Orogenic Belt extends westward to the Alxa Block, including the 1.9 Ga Bayan Obo mélange (Kusky et al., 2016; Wu et al., 2018), the Yinshan Block, and the Khondalite Belt at the northern margin of the North China Craton. Recent studies suggest that the 1.9–1.8 Ga granulite facies metamorphism in the Inner Mongolia-Jibei Orogenic Belt resulted from the convergence of the Columbia supercontinent (Kusky et al., 2016; Kusky and Traore, 2023). This interpretation is backed by evidence of 1904–1822 Ma high-pressure granulite facies metamorphism in the western Alxa Block (Wan B. et al., 2015) and ~1.9 Ga granulite facies metamorphism in the Bayan Obo mélange (Wu et al., 2018).

Along the southern margin of the Inner Mongolia-Jibei Orogenic Belt lies the Khondalite Belt, a 1,000 km long and 150–200 km wide east-west trending granulite facies metamorphic belt, referred to as the Khondalite Belt (Condie et al., 1992). It consists of sedimentary protoliths and is also known as the Fengzhen Orogenic Belt (Zhai and Peng, 2007), and alternatively as the Inner Mongolia Suture (Santosh, 2010) (Figure 1A). The Khondalite Belt primarily comprises rocks of the Khondalite series, such as garnet-sillimanite-bearing pelitic granulites, quartz-feldspar-garnet-biotite gneisses, marbles, and calc-silicate rocks. Traditionally, Khondalite is defined by two criteria: its protolith consists of aluminous sedimentary rocks, and it contains aluminous metamorphic minerals like sillimanite and garnet (Zhai, 2022), both of which are found in the Khondalite at the northern margin of the North China Craton. Charnockites and metamorphic gabbros presents within the Khondalite Belt and are intruded by S-type granites dated between 2.0–1.9 Ga (Kusky and Santosh, 2009; Li et al., 2022; Lian et al., 2022). Previous studies investigated the Khondalite Belt by structural, metamorphic, geochemical, geochronological, and geophysical methods. However, debate persists regarding the depositional environment of the Khondalite series protoliths (Zhai and Santosh, 2011; Santosh et al., 2013; Zhai and Santosh, 2013; Zhao and Zhai, 2013; Li et al., 2022; Yin et al., 2023), with arguments for both a stable continental margin (Condie et al., 1992; Wan et al., 2000) and an active continental margin (Dan et al., 2012; Cai et al., 2016; Li et al., 2022; Yin et al., 2023). Detrital zircons from the Khondalite series are primarily aged between 2.2–2.0 Ga, with some dating back to ~2.5 Ga (Wan et al., 2006; Dan et al., 2012). These rocks underwent metamorphism and anatexis during the late Paleoproterozoic, from 1.95 to 1.83 Ga (Wan et al., 2006; Dong et al., 2007; Shi et al., 2023). The 1.93–1.90 Ga metamorphic anatexis primarily occurred in the Jining-Liangcheng area, involving ~1.92 Ga ultra-high temperature granulites in Tuguiwula, ~1.93 Ga metamorphic gabbro-norites in the Liangcheng area (Santosh et al., 2007b; Peng et al., 2010; Wang L. J. et al., 2021), and 1.93–1.90 Ga *in-situ* to para-in-situ garnet granites resulting from Khondalite series anatexis (Peng et al., 2010; Wang et al., 2018).

The ultramafites are situated in the central-eastern part of the Inner Mongolia-Jibei Orogenic Belt. The exposed crystalline basement in this region primarily comprises the Paleoarchean Xinghe Group, the Mesoarchean Wulashan Group, and the Neoarchean Sertengshan Group (BGMR, 2008) (Figure 1B). The Paleoarchean Xinghe Group consists of granulites, biotite-plagioclase gneisses, and quartzites. The lower strata of the Mesoarchean Wulashan Group comprise migmatized amphibolite gneisses and granulites, whereas the upper strata consist of quartzites, marbles, potassium feldspar granulites, and biotite schists. The Neoarchean Sertengshan Group comprises biotite

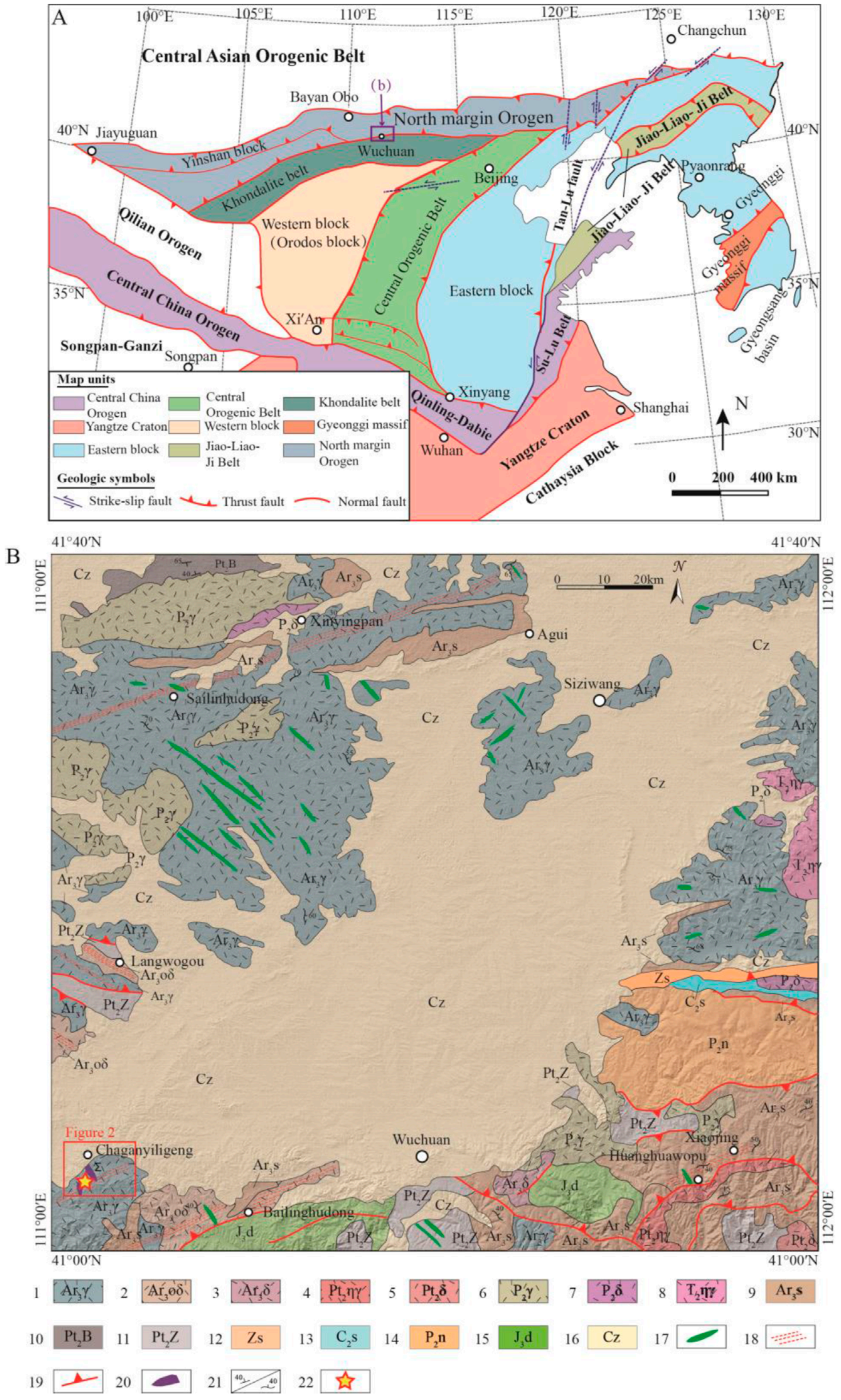

FIGURE 1
(A) North China Craton tectonic unit [modified from Wu et al. (2018)] **(B)** Regional geological map of Wuchuan area, Inner Mongolia. Note: 1. Neoarchean gneissic granite 2. Neoarchean quartz diorite 3. Neoarchean diorite 4. Mesoproterozoic monzogranite 5. Mesoproterozoic diorite 6. Late Permian granite 7. Late Permian diorite 8. Middle Triassic monzogranite 9. Neoarchean Seertengshan Group 10. Mesoproterozoic Bayan Obo Group 11. Mesoproterozoic Zhaertaishan Group 12. Sinian Shinagan Group 13. Intermediate Carboniferous Shuanmazhuang Fm 14. Lower Permian Naobaogou Fm 15. Upper Cretaceous Daqingshan Fm 16. Cenozoic-Quaternary sedimentary 17. mafic dike 18. shear zone 19. thrust fault 20. ultramafites 21. attitude of rock mass 22. Samples.

amphibolites, magnetite quartzites, quartz schists, marbles, and biotite hornfels. The Paleoproterozoic Baoyintu Group and Hongqiyingzi Group, along with the Khondalite Belt, have similar rock assemblage characteristics. The Baoyintu Group comprises metamorphic rocks ranging from upper greenschist to lower amphibolite facies, including quartzites, marbles, schists, and layered marble lenses (BGMR, 2008). The Hongqiyingzi Group comprises migmatized biotite amphibole-plagioclase rocks, biotite-plagioclase gneisses (Wang et al., 2011; Ge et al., 2016), sericite quartz schists, plagioclase amphibolites, and marbles. The northern margin of the North China Craton also includes widely distributed high-pressure granulite to amphibolite facies igneous rocks. These rocks formed during Neoarchean subduction magmatism and Paleoproterozoic extension (Wan B. et al., 2015; Wan Y. S. et al., 2015; Wu et al., 2018; Han et al., 2020). The basement rocks are intruded by 1.78–1.72 Ga mafic dikes, 1.67–1.56 Ga mafic rocks, and 1.34–1.23 Ga gabbros, pyroxenites, and granites (Peng, 2015; Zhou et al., 2016; Zhou et al., 2018b; Han et al., 2020). The sedimentary cover comprises Mesoproterozoic to Neoproterozoic Bayan Obo Group marine metamorphosed sedimentary rocks, Late Paleozoic clastic rocks, volcanic-sedimentary rocks, and Mesozoic to Cenozoic lacustrine sedimentary rocks (Figure 2) (Zhou et al., 2018a; Zhou et al., 2018b; Liu et al., 2020).

Detailed mapping (Figures 2, 3) were conducted on the ultramafites in the Chaganyiligeng area, southwest of Wuchuan. Rock samples with well-exposed outcrops were collected for zircon U-Pb geochronology and geochemical analysis. Rock types exposed in the study area can be categorized into two groups: the Khondalite series and the ultramafites. The Khondalite series comprises migmatized sillimanite-garnet-K-feldspar gneiss and biotite/garnet-plagioclase-two-pyroxene granulite, mainly distributed in the eastern and southern parts of the study area (Figure 2). The migmatized sillimanite-garnet-K-feldspar gneiss appears deep yellow-brown in outcrops, with two sets of conjugate shear joints developed (Figure 4A), exhibiting gneissic and banded structures (Figures 4B, C). The biotite/garnet-plagioclase-two-pyroxene granulite often occurs as xenoliths at the margins of the ultramafites body, ranging in size from 0.08 m^3 to 32.7 m^3 (Figures 4A–C). The ultramafites comprise primarily hornblende-pyroxenite and serpentinized dunite, layered with various lithologies forming a cumulate structure (Figure 4D, E). Hornblende-pyroxenite appears deep black or dark brown with massive or banded structures (Figure 5A), primarily exposed in the central part of the study area. The dunite is greenish or pale yellow-white, with grid structure and block structure, showing significant serpentinization (Figure 4D). Three Paleoproterozoic dunite outcrops are observed in a southwest-northeast direction (Figure 2), occasionally containing Paleoproterozoic granulite inclusions. Together, these constitute an exposed ultramafites intrusive body, appearing as a small stock. The northwestern part of the body is intersected by a normal fault and overlain by Cretaceous clastic sedimentary strata. The rock body exhibits fault zones from subsequent faulting activities, extending approximately 8 km in a southwest-northeast direction (Figure 2). Fault breccias in the fault zone exhibit brecciated structures, with clastic textures (Figure 5B), indicating the fault resulted from later activity. Fieldwork revealed remnants of garnet-K-feldspar gneiss atop the ultramafites body, with exposed areas approximately 10–20 m^2 (Figures 5C, D). The condensation edge and baking edge of ultramafites and gneiss can be clearly observed in the field (Figure 5E), indicating that the ultramafites mass intruded into the Paleoproterozoic gneiss.

3 Samples and methods

Twenty-two samples were collected in this study. The sample locations are illustrated in Figures 2, 3. Two gneiss samples include migmatized sillimanite-garnet-K-feldspar gneiss ($D05\text{-}Tb_1$) and garnet-K-feldspar gneiss ($D05\text{-}TW_1$). Three granulite samples include biotite-plagioclase-two-pyroxene granulite ($D07\text{-}Tb_1$) and garnet-plagioclase-two-pyroxene granulite ($D08\text{-}Tb_1/D08\text{-}TW_1$). Seventeen ultramafites samples include highly serpentinized dunite ($D11\text{-}b_{1to3}/D12\text{-}YQ_{1to5}/D12\text{-}Tb_1$) and hornblende-pyroxenite ($D11\text{-}TW_{1\text{-}2}/D11\text{-}YQ_{1to5}/D11\text{-}Tb_1$). In this study, the age dating of ultramafites was recalculated using data from samples 19-WC-03(a) and 19-WC-01(c) as reported by Wu et al. (2023). The location of the hornblende-pyroxenite sample ($D11\text{-}TW_1$) corresponds to the sample 19-WC-03(a) as published. The sample locations of the highly serpentinized dunite ($D12\text{-}TW_1$) and the hornblende-pyroxenite from published data [19-WC-01(c)] are located in the southern and northern parts of the Wuchuan ultramafites, respectively. The lithology of sample 19-WC-01(c) is hornblende-pyroxenite, occurring as enclaves within the highly serpentinized dunite. The gradational change in olivine content at the contact boundary suggests co-crystallization of hornblende-pyroxenite and dunite, indicating they belong to different mineral phases within the same magmatic system.

Zircon collection and cathodoluminescence (CL) images were conducted at the Regional Geological Survey Institute of Hebei Province, using standard procedures for single mineral separation. The selected zircons were embedded in epoxy resin, then photographed under transmitted light, reflected light, and cathodoluminescence (CL). The zircons were polished to expose their interiors, then observed under a scanning electron microscope for cathodoluminescence (CL) imaging to document the microstructure. This microstructure provided the basis for selecting analysis points during zircon U-Pb isotope measurements. Zircon U-Pb dating was performed at Beijing Zhongke Mine Research Testing Technology Co., Ltd., using a Neptune-type LAMC-ICP-MS instrument with a 193 nm laser wavelength and a 35 μm spot diameter. TE-MORA and GJ-1 were used as external standards to correct for matrix effects. Data were processed using the ICP-MS Data Cal program (Liu et al., 2010), and age calculations as well as concordia plot generation were carried out using the Isoplot program (Ludwig, 2003).

Major and trace element compositions were performed at Beijing Zhongke Mining and Testing Technology Co., Ltd. All samples were ground to under 200 mesh and oven-dried. A 1 g sample was weighed, placed in a crucible, and heated at 1,000°C for 1 h to determine the Loss on Ignition (LOI). After that, 5.85 g of a mixed flux (lithium borate, lithium metaborate, and lithium fluoride) and 0.65 g of the sample were accurately weighed and placed into a platinum crucible. The mixture was evenly stirred, 2–3 drops of saturated ammonium bromide were added, and it was melted in a high-frequency fusion machine to form a uniform glass

10.3389/feart.2024.1508394

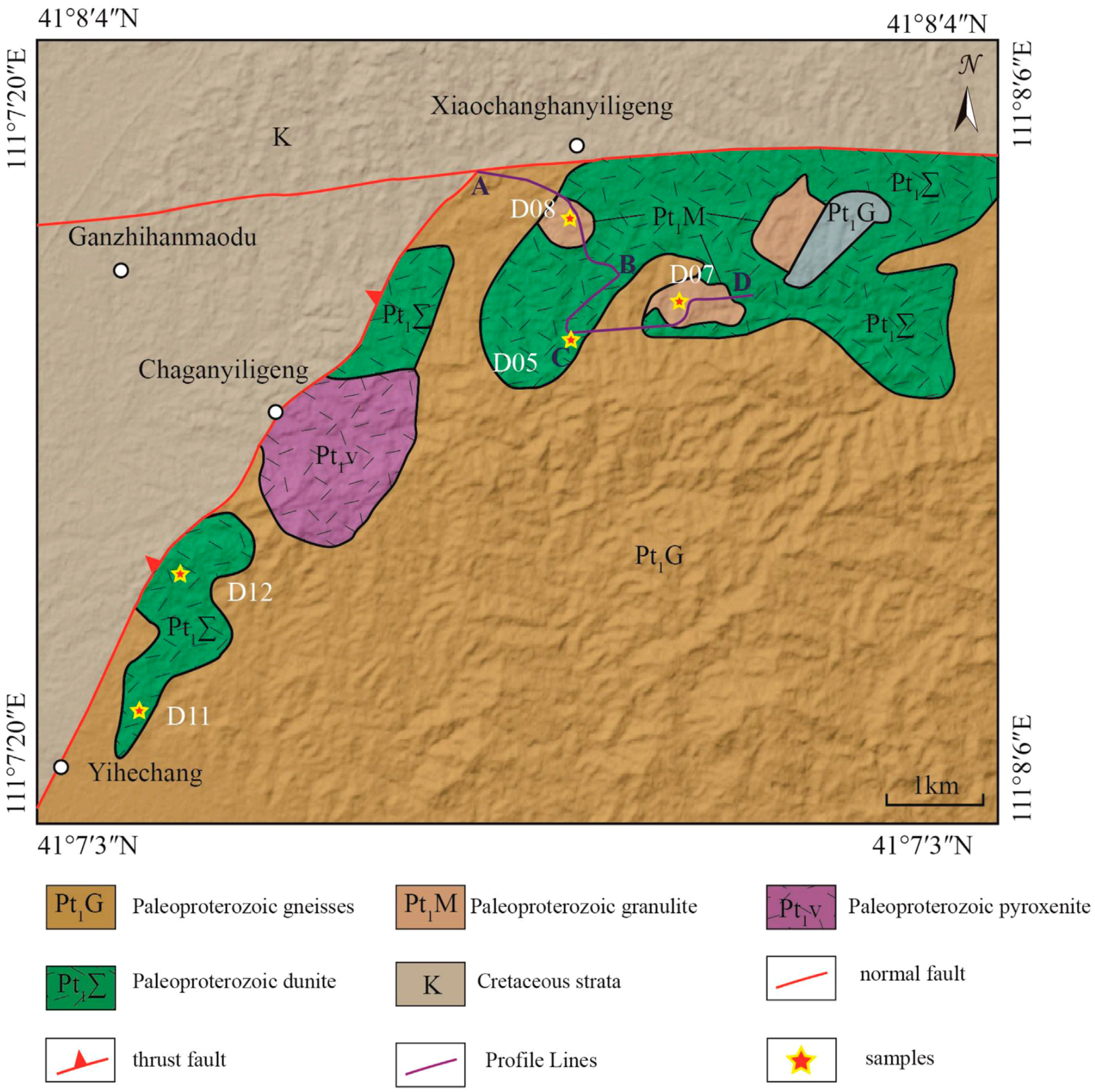

FIGURE 2
Geological map of the study area. **(A-D)** Represents the section position.

disc. Major elements were tested using a Shimadzu XRF-1800 X-ray fluorescence spectrometer, following the national standard GB/T 14,506.31–2019, with accuracy better than 2%. Trace and rare earth elements were analyzed using an Agilent 7500 ICP-MS (Inductively Coupled Plasma Mass Spectrometer) at Beijing Zhongke Mining and Testing Technology Co., Ltd. The main procedure was as follows: (1) Accurately weigh 50 mg of 200-mesh powdered sample and place it into a clean, air-dried Teflon digestion vessel. (2) Add 1 mL HF and heat to 150°C until completely dry. (3) Add 1.0 mL HF and 0.6 mL HNO_3, place the Teflon digestion vessel in a steel jacket, heat to 190°C, and maintain for over 96 h. Afterward, open the vessel and evaporate the solution to a milky droplet state to remove excess HF. (4) Add 1 mL concentrated HNO_3 and heat until it evaporates to a milky droplet state (repeat twice). (5) Add 1.6 mL HNO_3, and maintain the temperature at 140°C for 3–5 h. After cooling, transfer the sample to a 50 mL centrifuge tube, add 1 mL of 500 ng/g Rh internal standard, and dilute to 50 mL. (6) After thorough mixing, the solution was tested using an Agilent 7500 ICP-MS. The accuracy for most elements was better than 5%, while for lower-concentration elements, it ranged from 5% to 10%.

Mineral chemical analysis was performed in the EPMA laboratory at the Regional Geological Survey Institute of Hebei Province using a JEOL EPMA-8230 instrument. Testing conditions included an accelerating voltage of 15 kV and a probe current

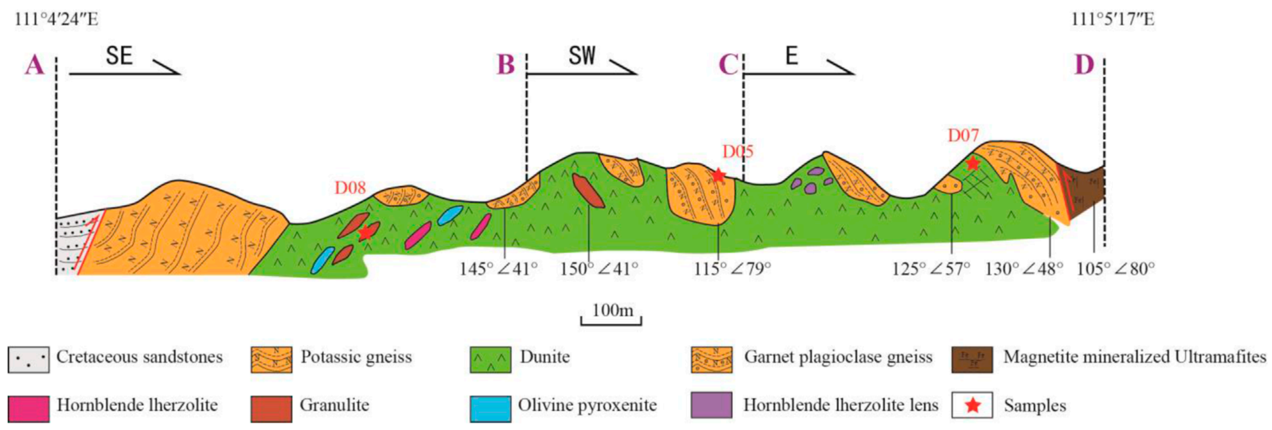

FIGURE 3
Cross-section showing contact relationships of geological bodies in the study area. **(A-D)** Represents the section position.

of 2 × 10^{-8} A. Mapping analysis utilized a probe current of 40 nA and an electron beam spot diameter of 5 μm. Natural and synthetic minerals were used as standards to calibrate elemental concentrations. Test data were corrected using the Zinc Application Framework (ZAF) method. The analytical error for major elements was below 1%, and mineral compositions were calculated using the Geokit program (Lu, 2004).

This study primarily employed five mineral geothermometers and three mineral geobarometers: the plagioclase-amphibole thermometer (Holland and Blundy, 1994), the two-pyroxene thermometer (Taylor, 1998), the clinopyroxene Ca thermometer (Xu, 1993), the garnet-clinopyroxene geothermometer (Raase, 2000), the garnet-orthopyroxene thermometer (Ashchepkov et al., 2017); the garnet-Al_2SiO_5-plagioclase-quartz (GASP) barometer (Holdaway, 2001), the garnet-orthopyroxene-plagioclase-quartz barometer (Lal, 1993; Simakov, 2012), and the amphibole total aluminum barometer (Hammarstrom and Zen, 1986; Mutch et al., 2016). The specific calculation processes are detailed in Supplementary Table S4.

4 Results

4.1 Petrograph

The sillimanite-garnet-K-feldspar gneiss (D05-Tb_1) (Figure 6A) exhibits a granoblastic texture with gneissic and banded structures. The rock is composed of a matrix (10%–15%) and veins (85%–90%). The matrix consists of K-feldspar (45%), plagioclase (5%–10%), quartz (20%), garnet (15%), sillimanite (5%–10%), and rutile (5%). Accessory minerals include opaque minerals and graphite; secondary minerals include sericite, clay, and allanite.

The biotite-plagioclase-pyroxene granulite (D07-Tb_1) (Figure 6B) is dark gray-black with a granoblastic texture and massive structure. The rock comprises diopside (65%), perilla pyroxene (10%), plagioclase (10%), biotite (10%), and amphibole (5%). Accessory minerals include opaque minerals.

The garnet-plagioclase-pyroxene granulite (D08-Tb_1) (Figure 6C) exhibits a granoblastic texture and massive structure. The rock consists of plagioclase (35%–40%), garnet (35%–40%), diopside (20%), perilla pyroxene (5%), and minor quartz. Limonite and carbonate-filled fractures are observed within the rock. Accessory minerals include opaque minerals. Secondary minerals are limonite, actinolite, and calcite.

The hornblende-pyroxenite (D11-Tb_1) (Figures 6D, E) has a columnar structure and massive texture. The rock is composed of clinopyroxene (55%), perilla pyroxene (5%), and hornblende (35%). The pyroxene is mainly clinopyroxene, followed by hypersthene, appearing as subhedral to anhedral columnar crystals, sized 1–4.5 mm. Accessory minerals include opaque minerals. Secondary minerals include actinolite.

The highly serpentinized dunite (D12-Tb_1) (Figure 6F) features a mesh texture and massive structure. The rock consists of pseudomorphs of olivine (nearly 100%) and minor pyroxene pseudomorphs. The olivine is granular, mostly serpentinized, with minor calcitization, appearing as pseudomorphs. Pyroxene is granular-columnar, replaced by calcite and minor serpentine as pseudomorphs, and is sparsely distributed. Accessory minerals include opaque minerals (5%–10%). Secondary minerals are predominantly serpentine.

4.2 Zircon U-Pb dating

The CL images of zircons from garnet-K-feldspar gneiss (D05-TW_1) (Figure 7A) show that most zircons are euhedral or subhedral. The zircon grain size ranges from 65 to 200 μm, with an aspect ratio of 1:1–1.8, and Th/U ratios between 0.01 and 1.27, with 40% of zircons having Th/U ratios greater than or equal to 0.4. Based on zircon characteristics, they can be divided into two groups: I and II. Group I zircons lack oscillatory zoning or core-rim structures and have rounded shapes, characteristic of metamorphic zircons. Group II zircons are partially lighter in color, lack distinct oscillatory zoning, often have dark inherited cores, and show significant metamorphic overprinting.

The CL images of zircons from garnet-plagioclase-two-pyroxene granulite (D08-TW_1) (Figure 7B) show that most zircons are subrounded, with a few being anhedral. The aspect ratio of zircons

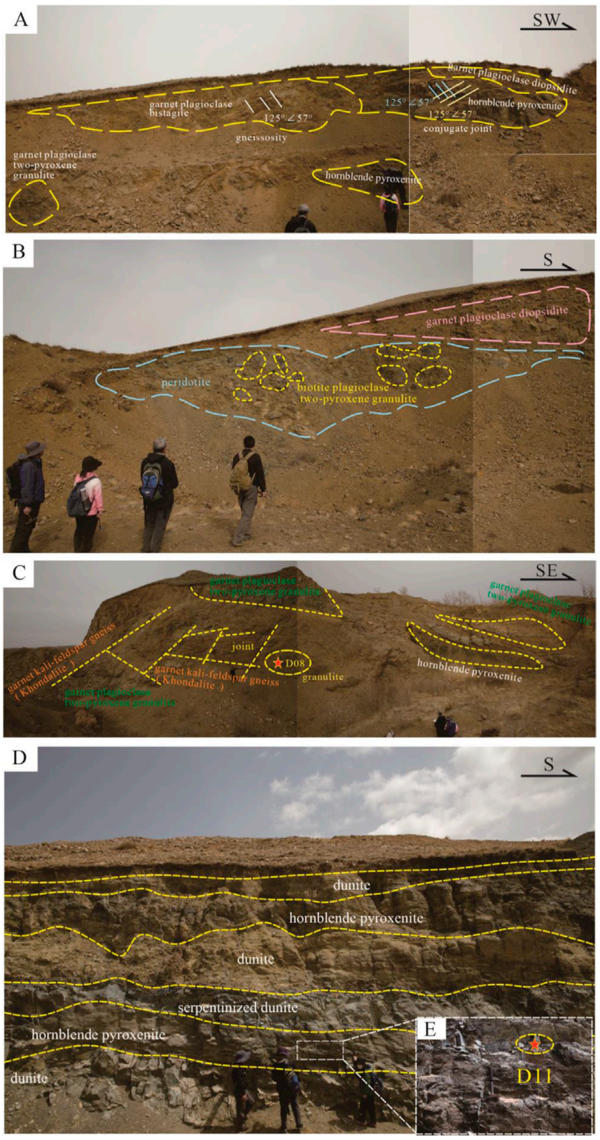

FIGURE 4
Characteristics of ultramafites and surrounding rocks **(A–C)**. Development of numerous granulite inclusions within the ultramafites body; **(D)** Layered Ultramafites with cumulate structures; **(E)** Field characteristics and sampling location of hornblende-pyroxenite).

ranges from 1:1 to 3:1, Th/U ratios range from 0.03 to 2.30, and grain sizes range from 40 to 150 μm, with four Th/U ratios less than 0.4. Based on zircon characteristics, they can be divided into three groups: I, II, and III. Group I zircons are darker in color, lack core-rim structures, or have typical oscillatory zoning with fir leaf-like zoning, characteristic of metamorphic zircons. Group II zircons are darker; some have dark centers with bright rims, and lack zoning, indicating metamorphic origins. Group III zircons are mostly brighter; some have inherited cores, and a few are darker with no or indistinct oscillatory zoning.

The CL images of zircons from hornblende-pyroxenite [D11-TW_1/19-WC-03(a)] (Figure 7C) show that most zircons are short prismatic, with a few being cylindrical. The zircons range in size from 20 to 150 μm, with an aspect ratio of 1:1 to 2:1, and Th/U ratios ranging from 0.04 to 1.81. About 50% of the zircons exhibit distinct oscillatory zoning, characteristic of magmatic zircons.

The serpentinized dunite [D12-TW_1/19-WC-03(c)] contains fewer zircons, and most zircon grains are small grains. The CL images (Figure 7D) show that the zircons are angular prismatic or rounded, with grain sizes ranging from 40 to 140 μm, aspect ratios from 1:1 to 5:1, and zoning structures. All zircons have Th/U ratios between 0.14 and 1.20, characteristic of magmatic zircons.

All the samples above selected age data with concordance rates between 90%–110%, with most age data points projecting on or near the concordia curve (Figure 8), indicating that the zircons tested were not significantly affected by later thermal events, with minimal Pb loss, suggesting high reliability of the dating results.

One hundred zircons from the garnet-K-feldspar gneiss (D05-TW_1) were selected for U-Pb testing, with results shown in Supplementary Table S1. Zircon ages are mainly distributed at two peaks: 2,200 Ma and 2,500 Ma, with the minimum age being 2,193 Ma and the maximum age 2,740 Ma (Figure 9A). The weighted average age of two Group I zircons is 2,193 ± 82 Ma (MSWD = 0.00, n = 2) (Figure 8A); the weighted average age of eight Group II zircons is 2,512 ± 37 Ma (MSWD = 0.97, n = 8). Given that the metamorphic mineral assemblage of the gneiss being typical of metasedimentary rocks, the protolith should be clastic rock. Therefore, the age distribution is complex. The smallest zircon age represents the metamorphic age of the garnet-K-feldspar gneiss at 2,193 ± 82 Ma, while the peak age of 2,512 ± 37 Ma may represent the protolith age.

One hundred zircons from the garnet-plagioclase-two-pyroxene granulite (D08-TW_1) were selected for U-Pb testing, with results shown in Supplementary Table S1. The minimum zircon age is 1,916 Ma, and the maximum age is 2,633 Ma. The zircon age frequency distribution histogram (Figure 9B) shows three peak ages at 1,950 Ma, 2,200 Ma, and 2,500 Ma. The weighted average age of three Group I zircons is 1,945 ± 71 Ma (MSWD = 0.19, n = 3) (Figure 8B); the weighted average age of eleven Group II zircons is 2,203 ± 80 Ma (MSWD = 0.15, n = 11); the weighted average age of sixty-one Group III zircons is 2,489 ± 24 Ma (MSWD = 0.62, n = 61). Analysis suggests that the youngest zircon age may represent the thermal contact metamorphism age, while older zircon ages may represent the protolith age of the granulite as a metasedimentary rock. Therefore, the age of 2,203 ± 80 Ma is considered the metamorphic age of the granulite, and the zircon age of 2,489 ± 24 Ma may represent the protolith age.

The zircon age data from the hornblende-pyroxenite [D11-TW_1/19-WC-03(a)] have a wide range, with the minimum age being 886 Ma and the maximum age 2,556 Ma (Figure 9C). The weighted average age of the 1,912–1,986 Ma interval is 1,947 ± 17 Ma (MSWD = 0.87, n = 15) (Figure 8C), which is considered to represent the crystallization age of the hornblende-pyroxenite. Ages around 2.5 Ga are likely the ages of zircons captured during magma ascent.

The minimum zircon age in the serpentinized dunite [D12-TW_1/19-WC-03(c)] is 290 Ma, and the maximum age is 2,580 Ma (Figure 9C). The youngest zircons may have lost Pb due to later metamorphic overprinting, while the oldest zircons likely represent ages of older country rocks captured later. Considering the field relationships between the harzburgite and hornblende-pyroxenite,

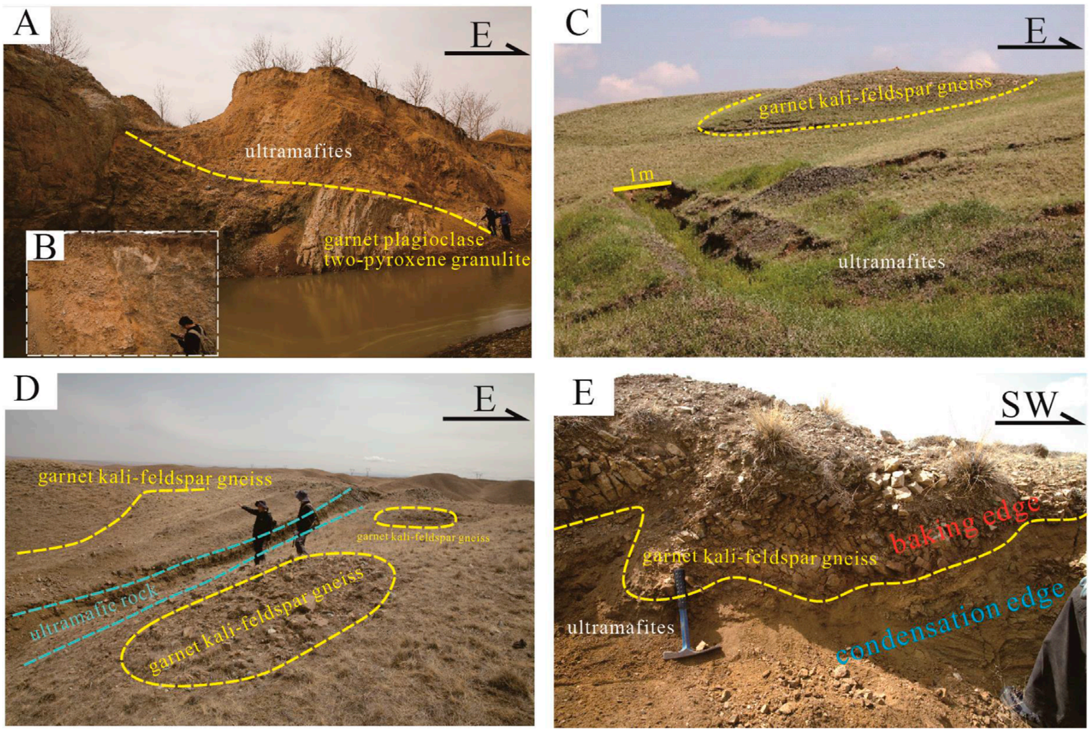

FIGURE 5
Relationship between ultramafites and surrounding rocks **(A, B)**. Plagioclase gneiss showing later fracturing and fault breccia characteristics; **(C, D)** Development of gneiss remnants on the Ultramafites body; **(E)** Intrusive contact relationship between gneiss and ultramafites).

the zircon age of 1,960 ± 25 Ma (Figure 8D) is deemed reliable, representing the crystallization age of the dunite.

4.3 Whole-rock geochemistry

4.3.1 Major elements

Supplementary Table S2 presents the results of major and trace element analyses for six samples. The Hornblende-pyroxenite (D11-YQ_{1to3}) has a major element composition with SiO_2 content ranging from 46.82% to 50.77%, averaging 48.9%, and high levels of TFe_2O_3 (12.92%–13.83%), MgO (16.28%–18.23%), and CaO (10.88%–12.63%). Major element discrimination diagrams show subalkaline tholeiitic characteristics (Figure 10). Na_2O content ranges from 0.69% to 1.39%, averaging 0.96%; K_2O content ranges from 0.22% to 0.61%, averaging 0.56%; TiO_2 content ranges from 0.27% to 0.7% (Supplementary Table S2); P_2O_5 content ranges from 0% to 0.19%, averaging 0.07%. The low $Mg^{\#}$ index (69.98–73.65) indicates minimal partial melting.

Serpentinized dunite (D12-YQ_{1to3}) has low SiO_2 content ranging from 35.79% to 36.7%, averaging 36.32%, with high TFe_2O_3 (14.73%–15.06%) and MgO (34.72%–35.77%), and low CaO content (0.07%–1.07%). Major element discrimination diagrams show subalkaline tholeiitic characteristics (Figure 10). It contains negligible amounts of Na_2O, K_2O, or P_2O_5 (content < 0.01%); TiO_2 content ranges from 0.01% to 0.02%. The $Mg^{\#}$ index is low, ranging from 82.03 to 82.79.

4.3.2 Trace elements

The rare earth element (REE) content in hornblende-pyroxenite (D11-YQ_{1to3}) is relatively low, ranging from 88.44 ppm to 113.79 ppm, with an average of 102.13 ppm. In the chondrite-normalized REE diagram (Figure 11A), hornblende-pyroxenite (D11) samples exhibit slight enrichment in light REEs [$(La/Yb)_N$ = 0.99–2.87] and a relatively uniform distribution of heavy REEs [$(Gd/Yb)_N$ = 1.29–1.57], showing a slight Eu anomaly (δEu = 0.82–1.04). In the primitive mantle-normalized spider diagram for trace elements (Figure 11B), ultramafites samples of hornblende-pyroxenite (D11) show enrichment in large ion lithophile elements (LILEs) like Rb and K, and depletion in high field strength elements (HFSEs) such as P, Zr, and Hf. The phosphorus (P) content in hornblende-pyroxenite D11-YQ_1 samples is notably lower compared to N-MORB (Sun and McDonough, 1989).

The REE content in serpentinized dunite (D12-YQ_{1to3}) is markedly lower than that in MORB and OIB (Sun and McDonough, 1989). In the chondrite-normalized REE diagram (Figure 11A), peridotite samples exhibit enrichment in light REEs [$(La/Yb)_N$ = 4.05–5.86] and a relatively uniform distribution of heavy REEs [$(Gd/Yb)_N$ = 0.94–1.32]. All three samples show slight negative Eu anomalies (δEu = 0.62–0.69). In the primitive mantle-normalized spider diagram for trace elements (Figure 11B), the samples show enrichment in large ion lithophile elements (LILEs) like Th and U, and depletion in high field strength elements (HFSEs) such as Nb, Zr, and Hf. Both hornblende-pyroxenite (D11-YQ_{1to3}) and peridotite (D12-YQ_{1to3}) samples exhibit Th/La ratios below 0.5,

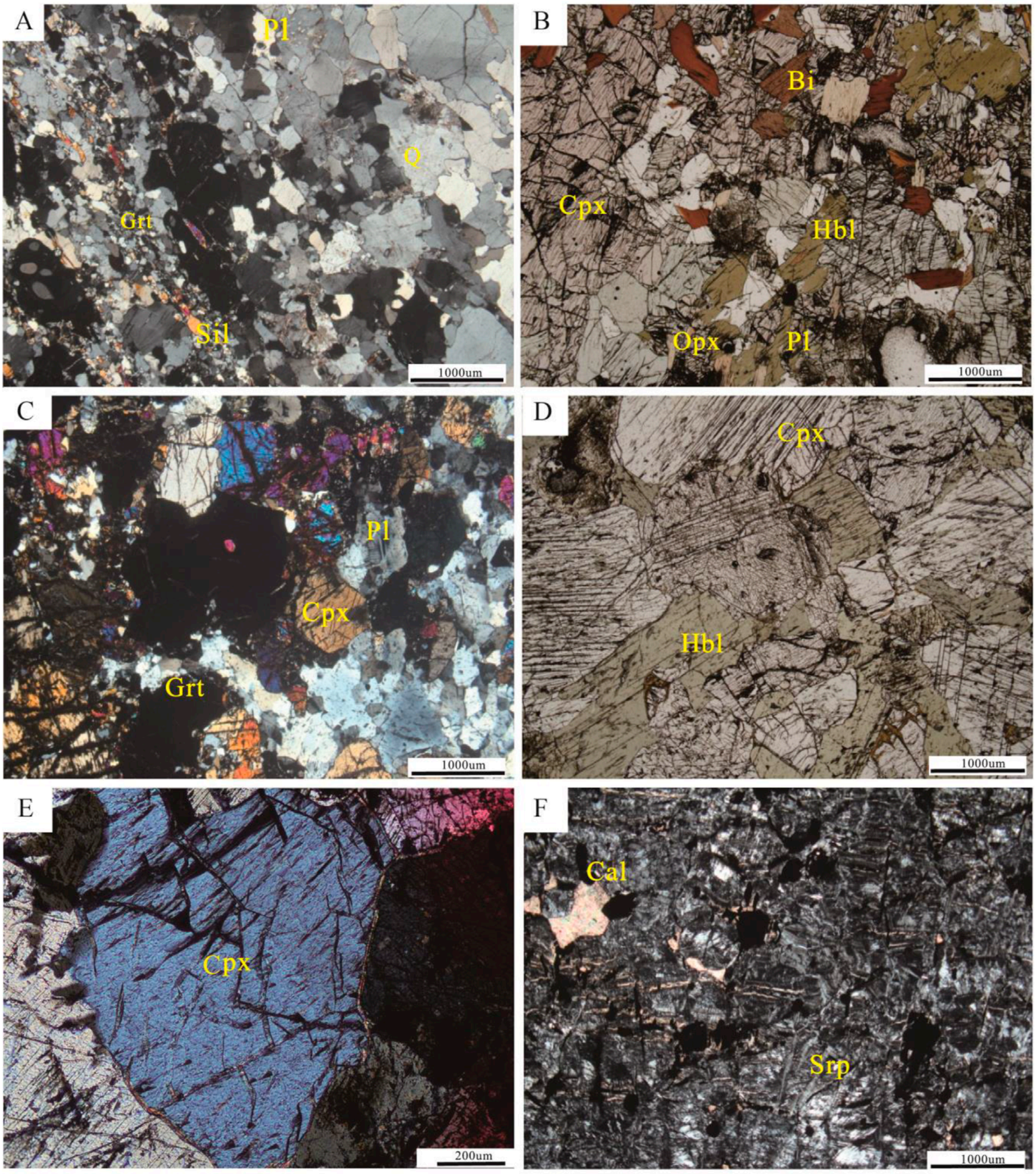

FIGURE 6
Mineral Photomicrographs of Samples. Note: **(A)** Migmatized sillimanite-garnet-K-feldspar gneiss (D05-Tb1); **(B)** Biotite-plagioclase-pyroxene granulite (D07-Tb1); **(C)** Garnet-plagioclase pyroxene granulite (D08-Tb1); **(D, E)** Hornblende pyroxenite (D11-Tb1); **(F)** Highly serpentinized dunite (D12-Tb1). Pl–Plagioclase; Q–Quartz; Sil–Sillimanite; Grt–Garnet; Cpx–Clinopyroxene; Opx–Orthopyroxene; Hbl–Hornblende; Cal–Carbonate; Srp–Serpentine.

which show a negative correlation with Sm/La, suggesting mantle-derived magmatic characteristics (Wang Y. et al., 2021).

4.4 Electron microprobe

This study conducted electron microprobe experiments on migmatized sillimanite-garnet-K-feldspar gneiss (D05-Tb_1), biotite-plagioclase-two-pyroxene granulite (D07-Tb_1), and garnet-plagioclase-two-pyroxene granulite (D08-Tb_1) from the Khondalite series, as well as hornblende-pyroxenite (D11-Tb_1) and strongly serpentinized peridotite (D12-Tb_1) from the Ultramafites. A total of 218 points were tested, with the experimental data and the positions of the test points shown in Supplementary Table S1.

Prior to performing temperature and pressure calculations, ensuring local rock mineral equilibrium is crucial, especially

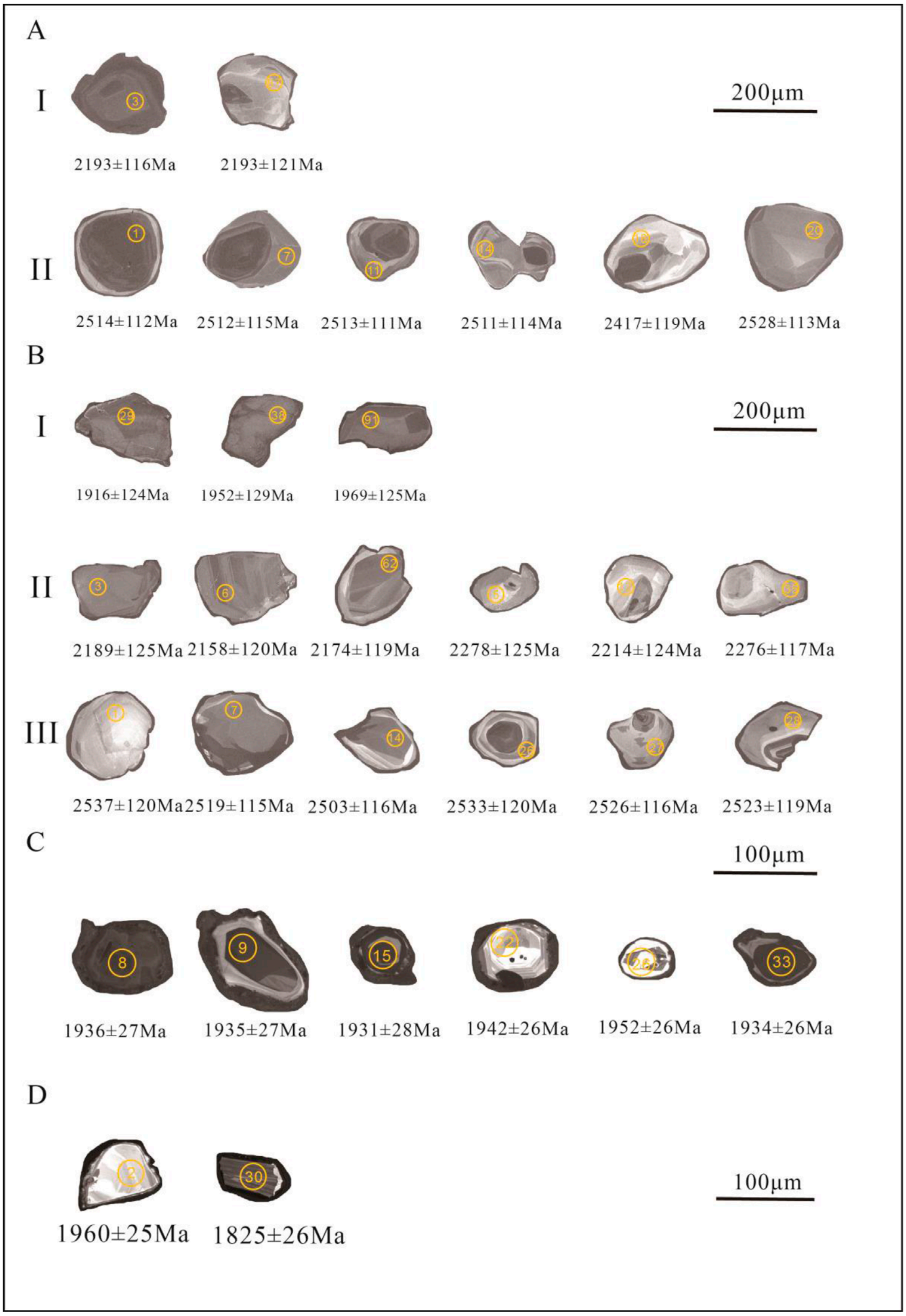

FIGURE 7
CL images of zircons from Wuchuan gneiss, granulite, hornblende-pyroxenite, and dunite (partial). **(A)** Migmatized sillimanite-garnet-K-feldspar gneiss (D05-TW1) zircon CL image; **(B)** Garnet-plagioclase pyroxene granulite (D08-TW1) zircon CL image; **(C)** Hornblende pyroxenite (D11-Tb1) zircon CL image; **(D)** Highly serpentinized dunite (D12-Tb1) zircon CL image.

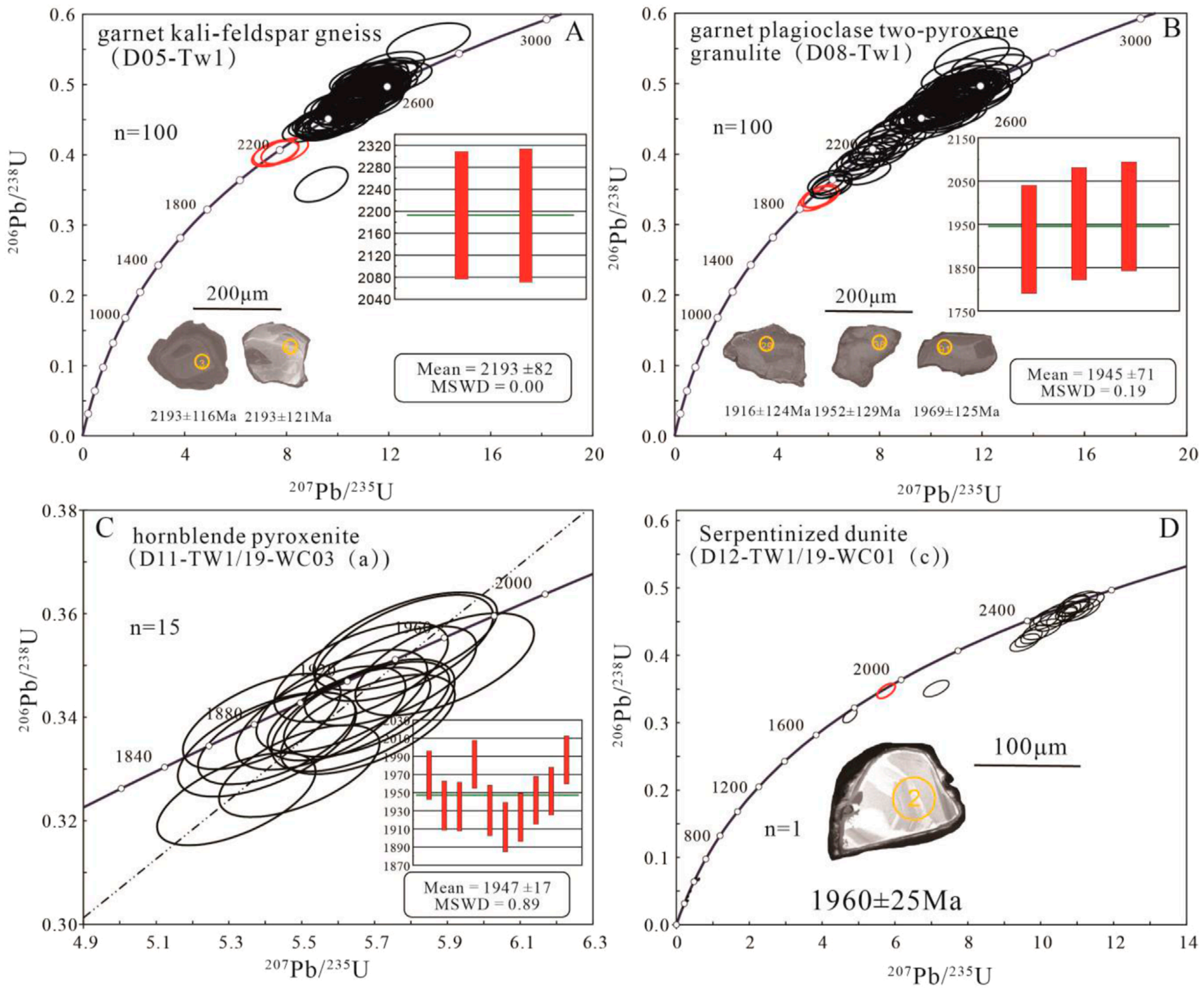

FIGURE 8
Concordia diagrams of zircon ages from Wuchuan, Inner Mongolia.

for applying specific geological mineral thermobarometers. This study utilized closely associated mineral pairs with fresh and well-defined mineral boundaries for thermobarometric calculations. Raw electron microprobe data were processed using the Geokit plugin (Lu, 2004) for individual mineral calculations of plagioclase, biotite, garnet, amphibole, and pyroxene. The processed data, including atomic and cation-anion numbers (Supplementary Table S3), were then used in the eight mineral thermobarometers detailed in Supplementary Table S5, yielding the experimental results presented in Supplementary Table S5.

5 Discussion

5.1 Ages of ultramafites

This study identified three zircon age groups—1.95 Ga, 2.2 Ga, and 2.5 Ga—in ultramafites, their surrounding rocks, and inclusions in the Wuchuan area (Figure 9). Most trace elements in the 2.5 Ga zircon align with magmatic zircons (Hoskin, 2005; Figure 12), while trace elements in garnet-potassium gneiss (D05-TW$_1$) and granulite (D08-TW$_1$) at 1.95 Ga and 2.2 Ga suggest metamorphic zircon origins (Hoskin, 2005; Zhong et al., 2018). The U-Pb age of magmatic zircon in hornblende pyroxenite from ultramafites is 1,947 ± 17 Ma, whereas no fresh samples could be obtained from the serpentinized dunite (D12-TW$_1$) due to severe weathering. In this study, the magmatic zircon U-Pb age of the inclusion [hornblende pyroxenite, 19-WC-01(c)] within the serpentinized dunite is 1960 ± 25 Ma. The two show clear stacking structural characteristics in the field (Figure 4D). Therefore, the 1,960 ± 25 Ma age of the hornblende pyroxenite is comparable to the crystallization age of the dunite. These two ages suggest magmatic crystallization occurred around ~1,950 Ma. These ages align with the development of peraluminous magmatism around 1,950 Ma in neighboring areas. Previous studies summarized that the northern margin of the North China Craton, along the Jining-Liangcheng-Qilianshan region, is characterized by abundant S-type granites (1,904–1,921 Ma) (Zhong et al., 2007). The formation age of

10.3389/feart.2024.1508394

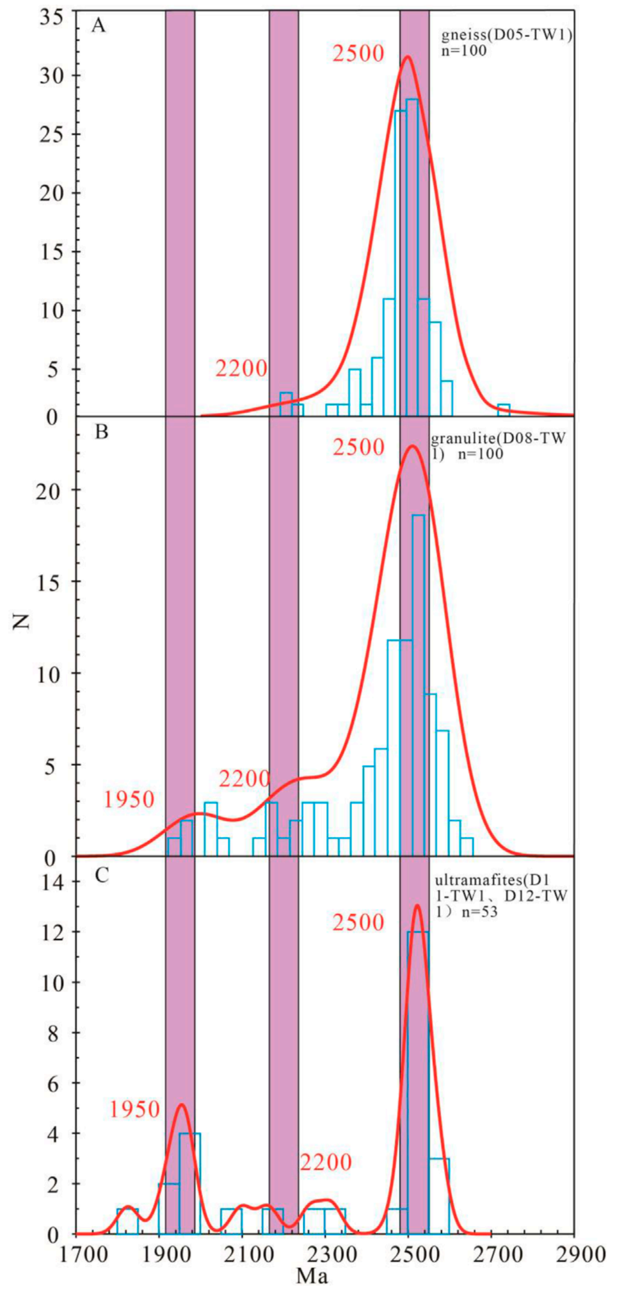

FIGURE 9
Frequency distribution histograms of zircon U-Pb ages.

garnet granite in Liangcheng is 1.93–1.92 Ga (Wang et al., 2018; Huang et al., 2019). During the same period, the Daqingshan area also underwent mafic magmatism in an extensional environment around 1.97–1.92 Ga, likely due to mantle magma underplating resulting in HT-UHT metamorphism (Wan et al., 2013). The 22 zircons in the 2,041–2,580 Ma range within the ultramafites are inherited zircons, preserving the ages of older surrounding rocks.

Field geological characteristics indicate that Wuchuan ultramafites intruded into Paleoproterozoic garnet-K-feldspar gneiss, with garnet-plagioclase-two-pyroxene granulite occurring as inclusions within them (Figures 5C, D). The CL images of zircons from garnet-K-feldspar gneiss reveal two types, with age peaks at 2,193 ± 82 Ma and 2,512 ± 37 Ma. Garnet-plagioclase-two-pyroxene granulite (D08-TW_1) displays three age peaks at 1,945 ± 71 Ma, 2,203 ± 80 Ma, and 2,489 ± 24 Ma (Figure 9). The ~2,500 Ma zircons in both rocks resemble the sedimentary age of the Khondalite protolith (Wan et al., 2006; Dan et al., 2012). The mineral assemblage of migmatized sillimanite-garnet-K-feldspar gneiss exhibits characteristics typical of metasedimentary rocks in the Khondalite series (Zhai, 2022). Therefore, the ~2,500 Ma ages represent the provenance ages of the protoliths of garnet-K-feldspar gneiss and garnet-plagioclase-two-pyroxene granulite. Zircon age distribution histograms (Figure 9) also depict peak ages of 2,200 Ma for both rocks, consistent with the metamorphic timing of the Khondalite series in the region (Dong et al., 2013). Therefore, the result identifies the ~2,200 Ma age as the metamorphic age of these rocks, potentially associated with the collision of the northern North China Craton with other terranes (Kusky and Li, 2003; Lian et al., 2023).

The zircon ages of 2,512 ± 37 Ma in gneiss and 2,433 ± 32 Ma in granulite represent the provenance ages of the Khondalite series protolith (~2,500 Ma) (Wan et al., 2006; Dan et al., 2012). Zircon ages of 2,193 ± 82 Ma in gneiss and 2,203 ± 80 Ma in granulite represent regional metamorphic ages of the Khondalite series, consistent with the ~2,200 Ma metamorphic event, potentially linked to the convergence of the North China Craton with the Columbia supercontinent (Kusky and Li, 2003; Kusky and Santosh, 2009; Kusky and Traore, 2023). Ages of 1,947 ± 17 Ma for hornblende-pyroxenite and 1,960 ± 25 Ma for serpentinized harzburgite indicate the intrusion of ultramafites into the Khondalite series around ~1,950 Ma, marking the magmatic crystallization age. The age of 1,945 ± 71 Ma for granulite likely represents thermal contact metamorphism due to the intrusion of ultramafites.

5.2 Petrogenesis of ultramafites

Ultramafites in the Wuchuan area display low TiO_2, Al_2O_3, low alkali, and high iron characteristics, indicative of tholeiitic basalt traits formed through high-degree partial melting of mantle peridotite (Green, 1973). Hornblende-pyroxenite and strongly serpentinized peridotite exhibit similar geochemical characteristics to previously studied ultramafites (Wu et al., 2023) (Figure 11). Differences in trace element distribution result from magmatic crystallization differentiation. In the field, this is evident from interlayered peridotite and hornblende-pyroxenite, which display a cumulate structure (Figure 4D). Ultramafites typically contain numerous altered/metamorphic minerals (e.g., amphibole, serpentine), requiring evaluation of the effects of subsequent alteration/metamorphism on the rock's chemical composition. Studies indicate that certain elements (e.g., K and Na) are prone to compositional changes during subsequent alteration/metamorphism (Muecke et al., 1979; Middelburg et al., 1988), reflected in the generally low Na_2O and K_2O values of the samples. Conversely, Al, Ca, and Mg remain relatively stable during subsequent alteration/metamorphism, preserving the original rock's

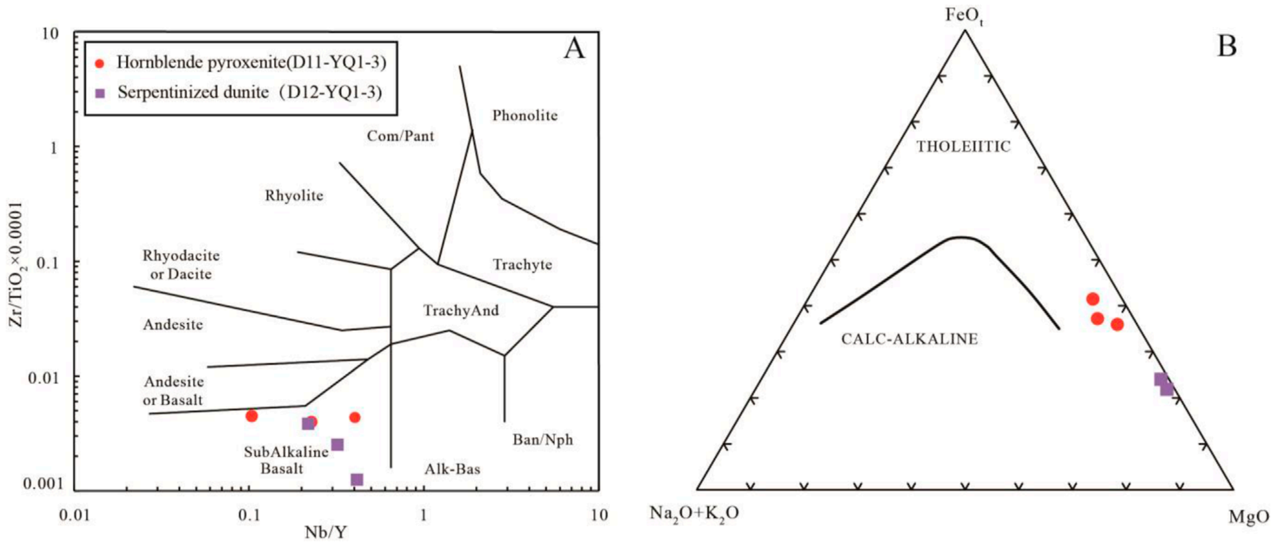

FIGURE 10
Nb/Y-Zr/TiO2×0.0001 diagram [**(A)** after (Winchester and Floyd, 1977)] and (Na2O+K2O)- FeOt-MgO (AFM) diagram [**(B)** after (Irvine and Baragar, 1971)] of ultramafites in the Wuchuan area.

geochemical characteristics. The geochemical characteristics of high field strength elements (Ti, Zr, Y, Nb, Ta, Hf, Th) and rare earth elements, which are minimally impacted by later alteration, can reveal the nature of the magma source in six ultramafite samples, aside from a few mobile elements.

Trace element ratios are effective indicators of elemental differentiation in magmatic processes and offer key insights into magma genesis (Weaver, 1991). The Th/La ratios in hornblende pyroxenite and peridotite samples are below 0.5 and negatively correlate with Sm/La, indicating a mantle-derived magma source (Wang Y. et al., 2021). Uncontaminated continental basalts generally have $(Th/Nb)_N < 1$ and $Nb/La > 1$, while crustal contamination results in $(Th/Nb)_N > 1$ and $Nb/La < 1$ (Saunders et al., 1988; Weaver, 1991). The $(Th/Nb)_{PM}$ ratios in the samples range from 0.04 to 6.29, averaging 2.28, while Nb/La ratios range from 0.14 to 0.93, averaging 0.55. The presence of older xenocrystic zircons in the ultramafites further suggests significant magmatic contamination. In the crustal contamination discrimination diagram (Figure 13), all ultramafite samples from Wuchuan fall within the crustal contamination field, suggesting that the magma underwent crustal contamination during ascent.

5.3 Relationship between ultramafites bodies and Khondalite series

The temperature and pressure conditions of the migmatized sillimanite-garnet-K-feldspar gneiss (D05-Tb_1) from the Khondalite series were determined to be 627°C and 7.6 kbar using the GASP barometer (Holdaway, 2001). The temperature and pressure conditions of the biotite-plagioclase-two-pyroxene granulite (D07-Tb_1) were determined to be 723°C and 6.3 kbar using multiple methods: amphibole total aluminum barometer (Hammarstrom and Zen, 1986; Mutch et al., 2016), plagioclase-amphibole thermometer (Holland and Blundy, 1994), two-pyroxene thermometer (Taylor, 1998), and clinopyroxene Ca thermometer (Xu, 1993). The temperature and pressure conditions of the garnet-plagioclase-two-pyroxene granulite (D08-Tb_1) were determined to be 599°C and 7.6 kbar using the garnet-orthopyroxene-plagioclase-quartz barometer (Lal, 1993; Simakov, 2012), garnet-clinopyroxene geothermometer (Raase, 2000), and garnet-orthopyroxene thermometer (Ashchepkov et al., 2017). The temperature and pressure conditions of the hornblende-pyroxenite (D11-Tb_1) from the Ultramafites were determined to be 768°C and 4.6 kbar using the amphibole total aluminum barometer (Hammarstrom and Zen, 1986; Mutch et al., 2016), two-pyroxene thermometer (Taylor, 1998), and clinopyroxene Ca thermometer (Xu, 1993).

The Khondalite Belt consists primarily of pelitic/felsic granulites, quartzites, calcsilicate rocks, and marbles (Lu and Jin, 1993; Zhai, 2022). It has experienced high-pressure (HP) and medium-pressure (MP) granulite facies metamorphism, as well as ultrahigh-temperature (UHT) granulite facies metamorphism. The Khondalite series in the Qilianshan, Helanshan, Daqingshan, Wulashan, and Jining areas underwent ~1.95 Ga HP granulite facies metamorphism, characterized by nearly isothermal decompression and clockwise P-T paths. Metamorphic zircon data concentrated around 1,950 Ma in the Khondalite Belt provide crucial evidence for continental collision (Yin et al., 2009; Cai et al., 2014; Xu et al., 2018; Wu et al., 2020; Yin et al., 2020). In the study area, 1.95 Ga ultramafites intruded into the Khondalite series, with field observations indicating that these ultramafites contain numerous granulite inclusions (Figures 4A–C). Mineral thermobarometric calculations (Supplementary Table S5) indicate that the gneiss and granulite in the study area formed under high-pressure and medium-temperature conditions, whereas

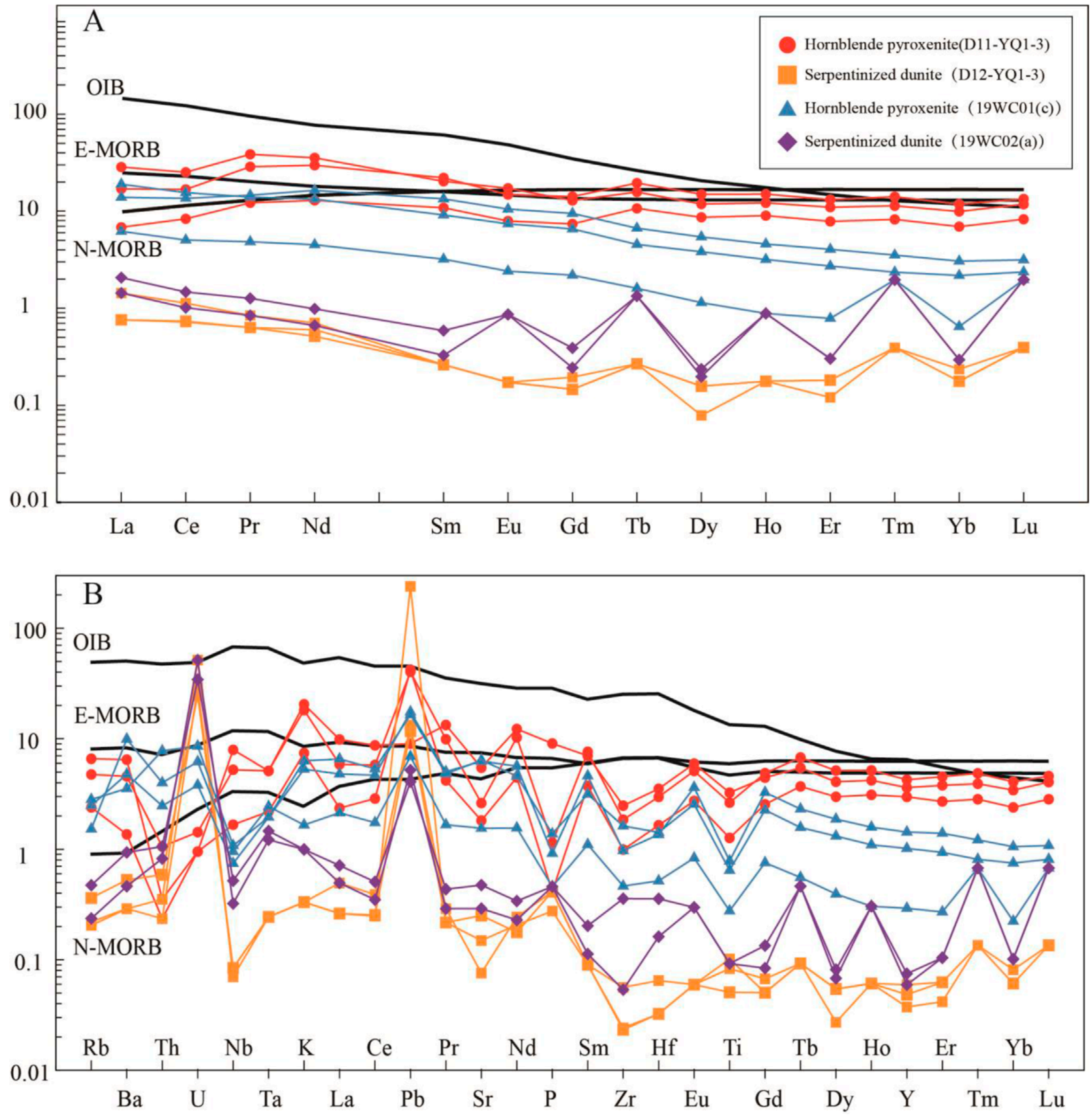

FIGURE 11
Normalization values are from (Sun and McDonough, 1989). **(A)** Chondrite-normalized curves; **(B)** Primitive mantle-normalized curves.

the ultramafites formed under medium-pressure and high-temperature conditions. The ultramafites intruded into the garnet-K-feldspar gneiss, suggesting that their formation conditions were insufficient to induce granulite facies metamorphism in the surrounding rocks.

5.4 Tectonic implications

The Khondalite Belt is acknowledged to have undergone a compressional event between 2.0 and 1.85 Ga; yet there remains substantial debate concerning its deformation phases and tectonic context. Kusky and Li (2003) and Lian et al. (2023) propose that metamorphism in the Khondalite Belt resulted from the collision of the northern North China Craton with other terranes between 2.2 and 1.85 Ga. Zhao (2009) proposes that the Khondalite Belt underwent two metamorphic events: one at 1.95 Ga due to the collision between the Ordos and Yinshan blocks, and another at 1.85 Ga due to the collision of eastern and western blocks. Zhai (2010) suggests that the North China Craton experienced a compressional orogeny event between 1.95 and 1.90 Ga, resulting in the metamorphism of the Khondalite Belt protoliths. Recent studies indicate that during the convergence of the North China Craton with the Columbia supercontinent, a significant Paleoproterozoic (2.3–1.8 Ga) collisional orogeny belt (the Inner Mongolia-Jibei orogenic belt) developed along its northern margin (Kusky and

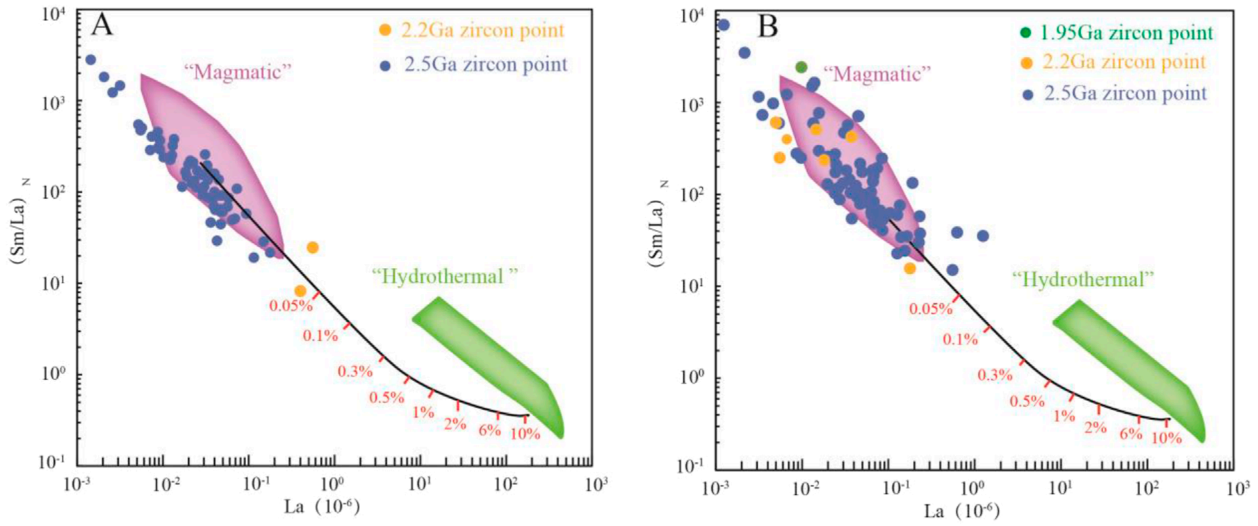

FIGURE 12
Zircon La-(Sm/La) N discrimination diagram base map is based on (Hoskin, 2005). **(A)** Migmatized sillimanite-garnet-K-feldspar gneiss (D05-TW1) zircon La-(Sm/La) N discrimination diagram; **(B)** Garnet-plagioclase pyroxene granulite (D08-TW1) zircon La-(Sm/La) N discrimination diagram.

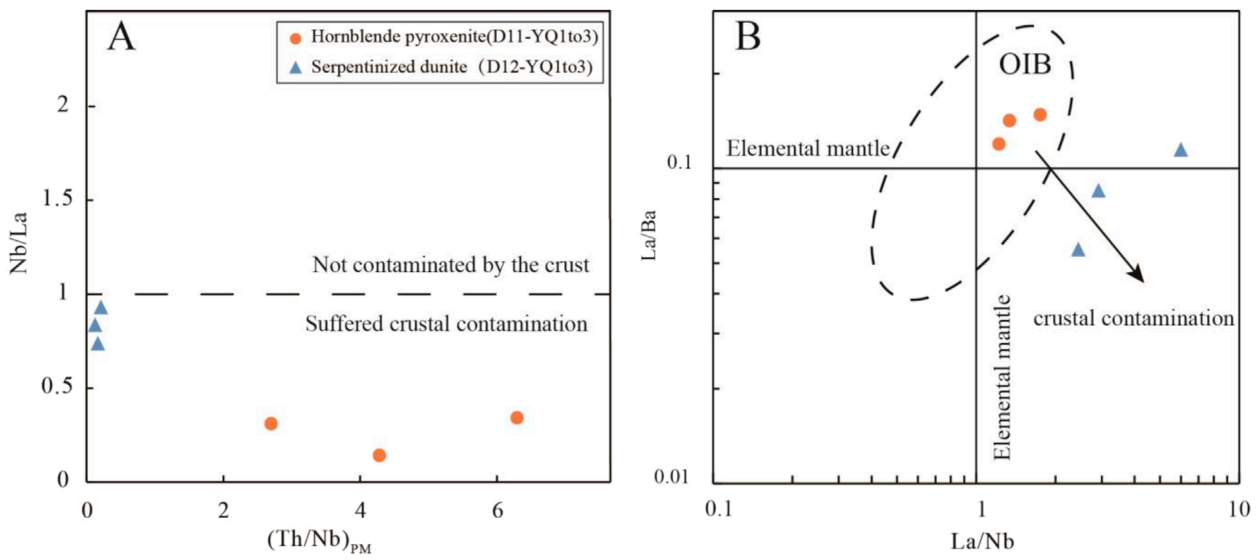

FIGURE 13
Ultramafites trace element covariation diagram base map is based on (Fitton et al., 1991). **(A)** (Th/Nb) PM-Nb/La discrimination diagram; **(B)** La/Nb-La/Ba discriminant diagram.

Li, 2003; Kusky and Santosh, 2009; Kusky and Traore, 2023). This belt formed through the amalgamation of the northern margin of the North China Craton with other cratons (Kusky et al., 2016) or the southwestern margin of the Siberian Craton (~2.3 Ga) (Wan B. et al., 2015; Wu et al., 2018). Subsequent magmatic activities related to orogeny occurred along the northern margin of the North China Craton between 1.87 and 1.78 Ga (Wu et al., 2022). Wu et al. (2018) propose that the 1980 Ma arc magmatic environment along the northern margin of the North China Craton was due to the southward subduction of the oceanic lithosphere at the southern margin of the Siberian Craton. The ~1.9 Ga emplacement of the Bayan Obo mélange along the northern margin of the North China Craton likely occurred during the Paleoproterozoic subduction and subsequent collision between the North China Craton and the Siberian Craton. The 2,200 Ma gneisses and granulites exposed in the Wuchuan area exhibit high-pressure, medium-temperature metamorphic conditions, indicative of a compressional environment. Ultramafites in the eastern Inner Mongolia–Northern Hebei orogenic belt formed under medium-pressure and high-temperature metamorphism.

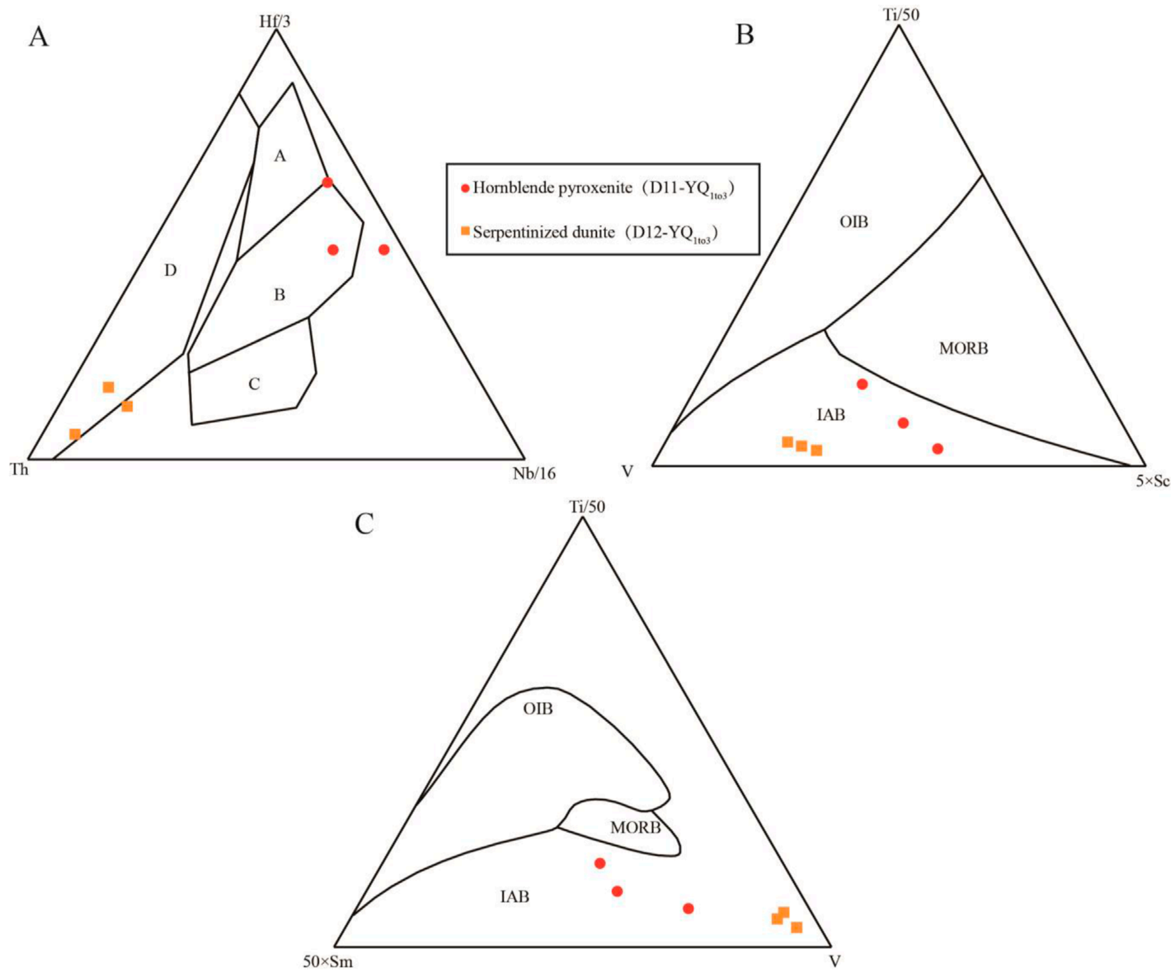

FIGURE 14
Tectonic Setting Discrimination Diagrams for Wuchuan Ultramafites. **(A)** A-N-type MORB, B-E-type MORB and within-plate tholeiitic basalts, C-alkaline within-plate basalts, D volcanic arc basalts; base map after (Wood, 1980); **(B, C)** base map after (Vermeesch, 2006) OIB Ocean Island Basalts, IAB-Island Arc Basalts, MORB- Mid-Ocean Ridge Basalts.

Tectonic discrimination diagrams (Figure 14) indicate that most samples fall within the island arc basalt field, revealing signs of crustal contamination. Field observations indicate a clear intrusive contact between ultramafites and surrounding gneisses. Hornblende pyroxenite and strongly serpentinized dunite within the ultramafites display clear cumulate structures, characteristic of mantle-derived magmatic rocks. The characteristics of the island arc may result from remnants of the subducted plate within the mantle. Thermobarometric calculations indicate that the ultramafites formed in a high-temperature, low-pressure environment. This study suggests that the ultramafites likely formed due to ongoing tectonic activity during the late stages of orogeny, which caused heat release from the crust and subsequent melting. Considering the regional geological background, the ultramafites are likely products of post-orogenic extensional settings. This environment resembles the ~1.9 Ga near east-west trending ultramafites (Han et al., 2020; Wu et al., 2022) and the 1,904–1,921 Ma peraluminous granite magmatic event (Wang et al., 2018; Huang et al., 2019), products of an extensional tectonic setting.

Previous studies have suggested that continent-continent collision and deep subduction in the Inner Mongolia-Jibei orogenic belt might have resulted in post-orogenic extensional collapse (Kusky and Li, 2003; Kusky et al., 2007b; Kusky and Santosh, 2009). This is illustrated by recently discovered mafic intrusions into granulite facies crust (Hou et al., 2008; Peng et al., 2010). The ultramafites in the Wuchuan area are also a result of this magmatic event. In conclusion, this study concludes that the metamorphism of the Khondalite series along the northern margin of the North China Craton coincided with orogenic events in the Inner Mongolia-Jibei orogenic belt, occurring by 2.2 Ga. Around 1950 Ma, post-orogenic extension saw ultramafite intrusions causing thermal contact metamorphism in the Khondalite series.

6 Conclusion

1) This study determined that the hornblende pyroxenite and serpentinized dunite in the Wuchuan area were emplaced

around 1,950 Ma. Ages of 2.2 Ga and 2.5 Ga from the surrounding garnet-K-feldspar gneiss and garnet-plagioclase-two-pyroxene granulite represent the regional metamorphic age and the protolith deposition age of the Khondalite Belt, respectively.

2) The Wuchuan ultramafites show high TFeO/MgO ratios and Al_2O_3 content, with considerable variation in K_2O/Na_2O and CaO. The hornblende pyroxenite is enriched in large ion lithophile elements (Rb, K) but depleted in high field strength elements (P, Th). Conversely, the dunite is enriched in high field strength elements (Th, U, P) and depleted in large ion lithophile elements (Rb, Sr, Eu). Tectonic analysis suggests these ultramafites formed during post-orogenic extension.
3) The gneiss formed at 626.85°C and 7.57 kbar, typical of high-pressure, medium-temperature conditions. The granulite formed at 599.29°C–723.42°C and 6.29–7.56 kbar, also under high-pressure, medium-temperature conditions. By contrast, the ultramafites formed at 767.93°C and 4.61 kbar, indicating a medium-pressure, high-temperature environment. The ultramafites intrusion did not cause granulite-facies metamorphism in the Khondalite, suggesting that the granulite metamorphism in the Khondalite Belt is not directly related to post-orogenic extension in the Inner Mongolia-Northern Hebei orogenic belt.

Data availability statement

The original contributions presented in the study are included in the article/Supplementary Material, further inquiries can be directed to the corresponding author.

Author contributions

HH: Conceptualization, Data curation, Investigation, Methodology, Software, Validation, Visualization, Writing - original draft, Writing–review and editing. DZ: Investigation, Methodology, Validation, Writing–review and editing. ZZ: Conceptualization, Data curation, Funding acquisition, Investigation, Resources, Supervision, Validation, Writing–review and editing. GW: Conceptualization, Funding acquisition, Investigation, Methodology, Project administration, Resources, Validation, Writing–review and editing. SG: Formal Analysis, Investigation, Supervision, Validation, Writing–review and editing. JC: Investigation, Methodology, Validation, Writing–review and editing. CF: Formal Analysis, Investigation, Methodology, Validation, Writing–review and editing.

Funding

The author(s) declare that financial support was received for the research, authorship, and/or publication of this article. This research was financially supported by the National Science Foundation of China: Early Paleozoic tectonic framework and evolution in the southern margin of western Xing-Meng Orogenic Belt (42272239).

Conflict of interest

The authors declare that the research was conducted in the absence of any commercial or financial relationships that could be construed as a potential conflict of interest.

Generative AI statement

The author(s) declare that no Generative AI was used in the creation of this manuscript.

Publisher's note

Supplementary material

The Supplementary Material for this article can be found online at: https://www.frontiersin.org/articles/10.3389/feart.2024.1508394/full#supplementary-material

References

Ashchepkov, I. V., Ntaflos, T., Logvinova, A. M., Spetsius, Z. V., Downes, H., and Vladykin, N. V. (2017). Monomineral universal clinopyroxene and garnet barometers for peridotitic, eclogitic and basaltic systems. *Geosci. Front.* 8, 775–795. doi:10.1016/j.gsf.2016.06.012

BGMR (2008). "Regional geology of inner mongol autonomous region," in *Regional geology of Inner Mongolia province* (Beijing, China: Geological Publishing House).

Cai, J., Liu, F. L., and Liu, P. H. (2017). Paleoproterozoic multistage metamorphic events in Jining metapelitic rocks from the Khondalite Belt in the North China Craton: evidence from petrology, phase equilibria modelling and U–Pb geochronology. *J. Asian Earth Sci.* 138, 515–534. doi:10.1016/j.jseaes.2017.02.034

Cai, J., Liu, F. L., Liu, P. H., Liu, C. H., Wang, F., and Shi, J. R. (2014). Metamorphic P-T path and tectonic implications of pelitic granulites from the daqingshan complex of the khondalite belt, north China craton. *Precambrian Res.* 241, 161–184. doi:10.1016/j.precamres.2013.11.012

Cai, J., Liu, F. L., Liu, P. H., Wang, F., and Shi, Y. J. (2016). Geochemistry and its tectonic implications of the Wulashan-Daqingshan metapelites in Inner Mongolia. *Acta Petrol. Sin.* 32, 1980–1996. (in Chinese with English abstract).

Chen, X. H., Dong, S. W., Shi, W., Ding, W. C., Zhang, Y. P., Li, B., et al. (2022). Construction of the continental asia in phanerozoic: a review. *Acta Geol. Sin.* 96, 26–51. (in Chinese with English abstract). doi:10.1111/1755-6724.14867

Condie, K. C., Boryta, M. D., Liu, J. Z., and Qian, X. L. (1992). The origin of khondalites: geochemical evidence from the Archean to Early Proterozoic granulite belt in the North China craton. *Precambrian Res.* 59, 207–223. doi:10.1016/0301-9268(92)90057-u

Dan, W., Li, X. H., Guo, J. H., Liu, Y., and Wang, X. C. (2012). Integrated *in situ* zircon U–Pb age and Hf–O isotopes for the Helanshan khondalites in North China Craton: juvenile crustal materials deposited in active or passive continental margin? *Precambrian Res.* 222-223, 143–158. doi:10.1016/j.precamres.2011.07.016

Dong, C. Y., Liu, D. Y., Li, J. J., Wang, Y. S., Zhou, H. Y., Li, C. D., et al. (2007). Palaeoproterozoic Khondalite Belt in the western North China Craton: new evidence from SHRIMP dating and Hf isotope composition of zircons from metamorphic rocks in the Bayan Ul-Helan Mountains area. *Chin. Sci. Bull.* 52, 2984–2994. doi:10.1007/s11434-007-0404-9

Dong, C. Y., Wan, Y. S., Xu, Z. Y., Liu, D. Y., Yang, Z. S., Ma, M. Z., et al. (2013). SHRIMP zircon U-Pb dating of late Paleoproterozoic kondalites in the Daqing Mountains area on the North China Craton. *Sci. China Earth Sci.* 56, 115–125. doi:10.1007/s11430-012-4459-3

Fitton, J. G., James, D., and Leeman, W. P. (1991). Basic magmatism associated with Late Cenozoic extension in the western United States: compositional variations in space and time. *J. Geophys. Res. Solid Earth* 96, 13693–13711. doi:10.1029/91jb00372

Ge, S. S., Zhai, M. G., Li, T. S., Peng, P., Wang, H. Z., and Cui, X. H. (2016). Geochronology of the medium-and low-grade metamorphosed supracrustal rocks from northern Hebei: constraint on the Late Neoarchean tectonic evolution of the North China Craton. *Acta Petrol. Sin.* 32, 571–589. (in Chinese with English abstract).

Gou, L. L., Zi, J. W., Dong, Y. P., Liu, X. M., Li, Z. H., Xu, X. F., et al. (2019). Timing of two separate granulite-facies metamorphic events in the Helanshan complex, North China Craton: constraints from monazite and zircon U–Pb dating of pelitic granulites. *Lithos* 350-351, 105216. doi:10.1016/j.lithos.2019.105216

Green, D. H. (1973). Experimental melting studies on a model upper mantle composition at high pressure under water-saturated and water-undersaturated conditions. *Earth Planet. Sci. Lett.* 19, 37–53. doi:10.1016/0012-821x(73)90176-3

Guo, J. H., Peng, P., Chen, Y., Jiao, S. J., and Windley, B. F. (2012). UHT sapphirine granulite metamorphism at 1.93-1.92 Ga caused by gabbronorite intrusions: implications for tectonic evolution of the northern margin of the North China Craton. *Precambrian Res.* 222-223, 124–142. doi:10.1016/j.precamres.2011.07.020

Hammarstrom, J. M., and Zen, E.-a. (1986). Aluminum in hornblende: an empirical igneous geobarometer. *Am. Mineralogist* 71, 1297–1313.

Han, S. X., Wu, C., Zhou, Z. G., and Wang, G. S. (2020). Geology, geochemistry, and geochronology of the paleoproterozoic Donggouzi mafic-ultramafic complex: implications for the evolution of the North China craton. *Lithos* 366-367, 105567. doi:10.1016/j.lithos.2020.105567

Holdaway, M. J. (2001). Recalibration of the GASP geobarometer in light of recent garnet and plagioclase activity models and versions of the garnet-biotite geothermometer. *Am. Mineralogist* 86, 1117–1129. doi:10.2138/am-2001-1001

Holland, T., and Blundy, J. (1994). Non-ideal interactions in calcic amphiboles and their bearing on amphibole-plagioclase thermometry. *Contributions Mineralogy Petrology* 116, 433–447. doi:10.1007/bf00310910

Hoskin, P. W. O. (2005). Trace-element composition of hydrothermal zircon and the alteration of Hadean zircon from the Jack Hills, Australia. *Geochimica Cosmochimica Acta* 69, 637–648. doi:10.1016/j.gca.2004.07.006

Hou, G. T., Li, J. H., Yang, M. H., Yao, W. H., Wang, C. C., and Wang, Y. X. (2008). Geochemical constraints on the tectonic environment of the Late Paleoproterozoic mafic dyke swarms in the North China Craton. *Gondwana Res.* 13, 103–116. doi:10.1016/j.gr.2007.06.005

Huang, G. Y., Guo, J. H., Jiao, S. J., and Palin, R. (2019). What drives the continental crust to Be extremely hot so quickly? *J. Geophys. Res. Solid Earth* 124, 11218–11231. doi:10.1029/2019jb017840

Irvine, T. N., and Baragar, W. R. A. (1971). A guide to the chemical classification of common volcanic rocks: Canadian Journal of Earth Sciences (Revue Candienne des Sciences de la Terre), v. 8.

Jiao, S. J., and Guo, J. H. (2020). Paleoproterozoic UHT metamorphism with isobaric cooling (IBC) followed by decompression–heating in the Khondalite Belt (North China Craton): new evidence from two sapphirine formation processes. *J. Metamorph. Geol.* 38, 357–378. doi:10.1111/jmg.12525

Kusky, T. M. (2011). Geophysical and geological tests of tectonic models of the North China Craton. *Gondwana Res.* 20, 26–35. doi:10.1016/j.gr.2011.01.004

Kusky, T. M., and Li, J. H. (2003). Paleoproterozoic tectonic evolution of the North China craton. *J. Asian Earth Sci.* 22, 383–397. doi:10.1016/s1367-9120(03)00071-3

Kusky, T. M., Li, J. H., and Santosh, M. (2007a). The paleoproterozoic north Hebei orogen: north China craton's collisional suture with the Columbia supercontinent. *Gondwana Res.* 12, 4–28. doi:10.1016/j.gr.2006.11.012

Kusky, T. M., Polat, A., Windley, B. F., Burke, K. C., Dewey, J. F., Kidd, W. S. F., et al. (2016). Insights into the tectonic evolution of the North China Craton through comparative tectonic analysis: a record of outward growth of Precambrian continents. *Earth-Science Rev.* 162, 387–432. doi:10.1016/j.earscirev.2016.09.002

Kusky, T. M., and Santosh, M. (2009). "The Columbia connection in north China,", 323. London: Geoscience word, 49–71. doi:10.1144/sp323.3

Kusky, T. M., and Traore, A. (2023). A paradigm shift: north China craton's north margin orogen is the collisional suture with the Columbia supercontinent. *Geochem. Geophys. Geosystems* 24, e2022GC010797. doi:10.1029/2022gc010797

Kusky, T. M., Windley, B. F., and Zhai, M. G. (2007b). "Tectonic evolution of the North China Block: from orogen to craton to orogen," 280. London: Geoscience word, 1–34. doi:10.1144/sp280.1

Lal, R. K. (1993). Internally consistent recalibrations of mineral equilibria for geothermobarometry involving garnet–orthopyroxene–plagioclase–quartz assemblages and their application to the South Indian granulites. *J. Metamorph. Geol.* 11, 855–866. doi:10.1111/j.1525-1314.1993.tb00195.x

Li, W. X., Yin, C. Q., Lin, S. F., Li, W. J., Gao, P., Zhang, J., et al. (2022). Paleoproterozoic tectonic evolution from subduction to collision of the khondalite belt in north China: evidence from multiple magmatism in the qianlishan complex. *Precambrian Res.* 368, 106471. doi:10.1016/j.precamres.2021.106471

Li, X. H. (2021). The major driving force triggering breakup of supercontinent: mantle plumes or deep subduction? *Acta Geol. Sin.* 95, 20–31. (in Chinese with English abstract).

Li, X. W., and Wei, C. J. (2018). Ultrahigh-temperature metamorphism in the Tuguiwula area, khondalite belt, north China craton. *J. Metamorph. Geol.* 36, 489–509. doi:10.1111/jmg.12301

Li, Z. X., and Zhong, S. j. (2009). Supercontinent–superplume coupling, true polar wander and plume mobility: plate dominance in whole-mantle tectonics. *Phys. Earth Planet. Interiors* 176, 143–156. doi:10.1016/j.pepi.2009.05.004

Lian, G., Xu, Z., Ren, Y., Feng, F., and Xue, J. (2022). Middle paleoproterozoic tectonic setting of khondalite belt: evidence from ~2.2 Ga charnockite in zhuozi. *Acta Petrol. Sin.* 38, 676–692. (in Chinese with English abstract). doi:10.18654/1000-0569/2022.03.06

Lian, G. H., Xu, Z. Y., Liu, Z. H., Liu, J., Li, P. C., Gong, Y. D., et al. (2023). Neoarchean to paleoproterozoic tectonic evolution of the khondalite belt in the North China craton: constraints from ca. 2.5 Ga and ca. 2.1 Ga charnockites in zhuozi. *Precambrian Res.* 396, 107167. doi:10.1016/j.precamres.2023.107167

Liu, C. H., Zhao, G. C., Liu, F. L., Shi, J. R., and Ji, L. (2020). Detrital zircon records of late Paleoproterozoic to early Neoproterozoic northern North China Craton drainage reorganization: implications for supercontinent cycles. *GSA Bull.* 132, 2135–2153. doi:10.1130/b35506.1

Liu, P. H., Liu, F. L., Liu, C. H., Liu, J. H., Wang, F., Xiao, L. L., et al. (2014). Multiple mafic magmatic and high-grade metamorphic events revealed by zircons from metamafic rocks in the Daqingshan–Wulashan Complex of the Khondalite Belt, North China Craton. *Precambrian Res.* 246, 334–357. doi:10.1016/j.precamres.2014.02.015

Liu, S. J., Tsunogae, T., Li, W. S., Shimizu, H., Santosh, M., Wan, Y. S., et al. (2012). Paleoproterozoic granulites from Heling'er: implications for regional ultrahigh-temperature metamorphism in the North China Craton. *Lithos* 148, 54–70. doi:10.1016/j.lithos.2012.05.024

Liu, Y. S., Hu, Z. C., Zong, K. Q., Gao, C. G., Gao, S., Xu, J., et al. (2010). Reappraisement and refinement of zircon U-Pb isotope and trace element analyses by LA-ICP-MS. *Chin. Sci. Bull.* 55, 1535–1546. doi:10.1007/s11434-010-3052-4

Lu, L. Z., and Jin, S. Q. (1993). P-T-t paths and tectonic history of an early Precambrian granulite facies terrane, Jining district, south-east Inner Mongolia, China. *J. Metamorph. Geol.* 11, 483–498. doi:10.1111/j.1525-1314.1993.tb00166.x

Lu, Y. F. (2004). GeoKit: a geochemical toolkit based on vba. *Geochimica*, 459–464.

Ludwig, K. R. (2003). *User's manual for Isoplot 3.00: a geochronological toolkit for Microsoft Excel*. Ludwig: Kenneth R.

Middelburg, J. J., Van Der Weijden, C. H., and Woittiez, J. R. W. (1988). Chemical processes affecting the mobility of major, minor and trace elements during weathering of granitic rocks. *Chem. Geol.* 68, 253–273. doi:10.1016/0009-2541(88)90025-3

Muecke, G. K., Pride, C., and Sarkar, P. (1979). Rare-earth element geochemistry of regional metamorphic rocks. *Phys. Chem. Earth* 11, 449–464. doi:10.1016/0079-1946(79)90043-0

Murphy, J. B., and Nance, R. D. (2013). Speculations on the mechanisms for the formation and breakup of supercontinents. *Geosci. Front.* 4, 185–194. doi:10.1016/j.gsf.2012.07.005

Mutch, E. J. F., Blundy, J. D., Tattitch, B. C., Cooper, F. J., and Brooker, R. A. (2016). An experimental study of amphibole stability in low-pressure granitic magmas and a revised Al-in-hornblende geobarometer. *Contributions Mineralogy Petrology* 171, 85. doi:10.1007/s00410-016-1298-9

Nance, R. D. (2022). The supercontinent cycle and Earth's long-term climate. *Ann. N. Y. Acad. Sci.* 1515, 33–49. doi:10.1111/nyas.14849

Nance, R. D., Worsley, T. R., and Moody, J. B. (1988). The supercontinent cycle. *Sci. Am.* 259, 72–79. doi:10.1038/scientificamerican0788-72

Peng, P. (2015). Precambrian mafic dyke swarms in the North China Craton and their geological implications. *Sci. China Earth Sci.* 58, 649–675. doi:10.1007/s11430-014-5026-x

Peng, P., Guo, J. H., Windley, B. F., Liu, F., Chu, Z., and Zhai, M. G. (2012). Petrogenesis of late paleoproterozoic Liangcheng charnockites and S-type granites in the central-northern margin of the North China craton: implications for ridge subduction. *Precambrian Res.* 222-223, 107–123. doi:10.1016/j.precamres.2011.06.002

Peng, P., Guo, J. H., Zhai, M. G., and Bleeker, W. (2010). Paleoproterozoic gabbronoritic and granitic magmatism in the northern margin of the North China craton: evidence of crust–mantle interaction. *Precambrian Res.* 183, 635–659. doi:10.1016/j.precamres.2010.08.015

Raase, P. (2000). Orientation of exsolution lamellae and rods, and optimal phase-boundaries in antiperthite from pelitic granulites, Sri Lanka. *Can. Mineralogist* 38, 695–705. doi:10.2113/gscanmin.38.3.695

Santosh, M. (2010). Assembling North China Craton within the Columbia supercontinent: the role of double-sided subduction. *Precambrian Res.* 178, 149–167. doi:10.1016/j.precamres.2010.02.003

Santosh, M., Liu, D. Y., Shi, Y. R., and Liu, S. J. (2013). Paleoproterozoic accretionary orogenesis in the North China Craton: a SHRIMP zircon study. *Precambrian Res.* 227, 29–54. doi:10.1016/j.precamres.2011.11.004

Santosh, M., Tsunogae, T., Li, J. H., and Liu, S. J. (2007a). Discovery of sapphirine-bearing Mg-Al granulites in the North China Craton: implications for Paleoproterozoic ultrahigh temperature metamorphism. *Gondwana Res.* 11, 263–285. doi:10.1016/j.gr.2006.10.009

Santosh, M., Tsunogae, T., Ohyama, H., Sato, K., Li, J. H., and Liu, S. J. (2008). Carbonic metamorphism at ultrahigh-temperatures: evidence from north China craton. *Earth Planet. Sci. Lett.* 266, 149–165. doi:10.1016/j.epsl.2007.10.058

Santosh, M., Wilde, S. A., and Li, J. H. (2007b). Timing of paleoproterozoic ultrahigh-temperature metamorphism in the North China craton: evidence from SHRIMP U–Pb zircon geochronology. *Precambrian Res.* 159, 178–196. doi:10.1016/j.precamres.2007.06.006

Saunders, A. D., Norry, M. J., and Tarney, J. (1988). Origin of MORB and chemically-depleted mantle reservoirs: trace element constraints. *J. Petrology* Special_Volume, 415–445. Special_Volume. doi:10.1093/petrology/special_volume.1.415

Shi, Q., Li, C. Z., Yu, X., Gao, X., Li, H. X. M., Ren, W., et al. (2023). Geochemistry and geological significance of the two episodes of anatectic garnet granites in the khondalite belt, northern margin of the North China craton. *J. Jilin Univ. Sci. Ed.* 53, 1090–1116.

Simakov, S. K. (2012). A new garnet thermometer for mantle peridotites and estimation of the diamond potential on its basis. *Dokl. Earth Sci.* 445, 1003–1005. doi:10.1134/s1028334x12060189

Sun, S. S., and McDonough, W. F. (1989). "Chemical and isotopic systematics of oceanic basalts: implications for mantle composition and processes," 42. London: Geoscience word, 313–345. doi:10.1144/gsl.sp.1989.042.01.19

Taylor, S. R., and McLennan, S. M. (1995). The geochemical evolution of the continental crust. *Rev. Geophys.* 33, 241–265. doi:10.1029/95rg00262

Taylor, W. R. (1998). An experimental test of some geothermometer and geobarometer formulations for upper mantle peridotites with application to the thermobarometry of fertile lherzolite and garnet websterite. *Neues Jahrb. für Mineral. - Abh.* 172, 381–408. doi:10.1127/njma/172/1998/381

Vermeesch, P. (2006). Tectonic discrimination diagrams revisited. *Geochem. Geophys. Geosystems* 7, 2005GC001092. doi:10.1029/2005gc001092

Wan, B., Windley, B. F., Xiao, W. J., Feng, J. Y., and Zhang, J. E. (2015). Paleoproterozoic high-pressure metamorphism in the northern North China Craton and implications for the Nuna supercontinent. *Nat. Commun.* 6, 8344. doi:10.1038/ncomms9344

Wan, Y. S., Geng, Y. S., Shen, Q. H., and Zhang, R. X. (2000). Khondalite series-geochronology and geochemistry of the jiehekou group in luliang area. *Acta Petrol. Sin.* 16, 49–58. (in Chinese with English abstract).

Wan, Y. S., Song, B., Liu, D. Y., Wilde, S. A., Wu, J. S., Shi, Y. R., et al. (2006). SHRIMP U–Pb zircon geochronology of Palaeoproterozoic metasedimentary rocks in the North China Craton: evidence for a major Late Palaeoproterozoic tectonothermal event. *Precambrian Res.* 149, 249–271. doi:10.1016/j.precamres.2006.06.006

Wan, Y. S., Xu, Z. Y., Dong, C. Y., Nutman, A., Ma, M. Z., Xie, H. Q., et al. (2013). Episodic Paleoproterozoic (~2.45, ~1.95 and ~1.85Ga) mafic magmatism and associated high temperature metamorphism in the Daqingshan area, North China Craton: SHRIMP zircon U–Pb dating and whole-rock geochemistry. *Precambrian Res.* 224, 71–93. doi:10.1016/j.precamres.2012.09.014

Wang, B., Wei, C. J., Tian, W., and Fu, B. (2020). UHT metamorphism peaking above 1100 °c with slow cooling: insights from pelitic granulites in the jining complex, north China craton. *J. Petrology* 61, egaa070. doi:10.1093/petrology/egaa070

Wang, F., Chen, F. K., Siebel, W., Li, S. Q., Peng, P., and Zhai, M. G. (2011). Zircon U–Pb geochronology and Hf isotopic composition of the Hongqiyingzi complex, northern Hebei Province: new evidence for paleoproterozoic and late paleozoic evolution of the northern margin of the North China craton. *Gondwana Res.* 20, 122–136. doi:10.1016/j.gr.2011.02.003

Wang, L. J., Guo, J. H., and Peng, P. (2021). Petrogenesis of paleoproterozoic Liangcheng garnet granitoids in the khondalite belt, north China craton. *Acta Petrol. Sin.* 37, 375–390. (in Chinese with English abstract). doi:10.18654/1000-0569/2021.02.04

Wang, L. J., Guo, J. H., Yin, C. Q., Peng, P., Zhang, J., Spencer, C. J., et al. (2018). High-temperature S-type granitoids (charnockites) in the Jining complex, North China Craton: restite entrainment and hybridization with mafic magma. *Lithos* 320-321, 435–453. doi:10.1016/j.lithos.2018.09.035

Wang, Y., Foley, S. F., Buhre, S., Soldner, J., and Xu, Y. G. (2021). Origin of potassic postcollisional volcanic rocks in young, shallow, blueschist-rich lithosphere. *Sci. Adv.* 7, eabc0291. doi:10.1126/sciadv.abc0291

Wan Y. S., Y. S., Liu, D. Y., Dong, C. Y., Xie, H. Q., Kröner, A., Ma, M. Z., et al. (2015). "Formation and evolution of archean continental crust of the North China craton," in *Precambrian geology of China*. Editor M. ZHAI (Berlin, Heidelberg: Springer).

Weaver, B. L. (1991). The origin of ocean island basalt end-member compositions: trace element and isotopic constraints. *Earth Planet. Sci. Lett.* 104, 381–397. doi:10.1016/0012-821x(91)90217-6

Winchester, J. A., and Floyd, P. A. (1977). Geochemical discrimination of different magma series and their differentiation products using immobile elements. *Chem. Geol.* 20, 325–343. doi:10.1016/0009-2541(77)90057-2

Wood, D. A. (1980). The application of a Th Hf Ta diagram to problems of tectonomagmatic classification and to establishing the nature of crustal contamination of basaltic lavas of the British Tertiary Volcanic Province. *Earth Planet. Sci. Lett.* 50, 11–30. doi:10.1016/0012-821x(80)90116-8

Wu, C., Wang, G. S., Zhou, Z. G., Haproff, P. J., Zuza, A. V., and Liu, W. Y. (2022). Paleoproterozoic Plate tectonics recorded in the northern margin orogen, north China craton. *Geochem. Geophys. Geosystems* 23, e2022GC010662. doi:10.1029/2022gc010662

Wu, C., Wang, G. S., Zhou, Z. G., Zhao, X. Q., and Haproff, P. J. (2023). Late Archean–Paleoproterozoic plate tectonics along the northern margin of the North China craton. *GSA Bull.* 135, 967–989. doi:10.1130/b36533.1

Wu, C., Zhou, Z. G., Zuza, A. V., Wang, G. S., Liu, C. F., and Jiang, T. (2018). A 1.9-Ga mélange along the Northern margin of the North China craton: implications for the assembly of Columbia supercontinent. *Tectonics* 37, 3610–3646. doi:10.1029/2018tc005103

Wu, S., Yin, C., Davis, D. W., Zhang, J., Qian, J., Qiao, H., et al. (2020). Metamorphic evolution of high-pressure felsic and pelitic granulites from the Qianlishan Complex and tectonic implications for the Khondalite Belt, North China Craton. *Bull. Geol. Soc. Am.* 132, 2253–2266. doi:10.1130/b35502.1

Xiao, W. J., Windley, B. F., Sun, S., Li, J. L., Huang, B. C., Han, C. M., et al. (2015). A tale of amalgamation of three permo-triassic collage systems in central asia: oroclines, sutures, and terminal accretion. *Annu. Rev. Earth Planet. Sci.* 43, 477–507. doi:10.1146/annurev-earth-060614-105254

Xu, X. F., Gou, L. L., Long, X. P., Dong, Y. P., Liu, X. M., Zi, J. W., et al. (2018). Phase equilibrium modelling and SHRIMP zircon U–Pb dating of medium-pressure pelitic granulites in the Helanshan complex of the Khondalite Belt, North China Craton, and their tectonic implications. *Precambrian Res.* 314, 62–75. doi:10.1016/j.precamres.2018.05.030

Xu, Y. G. (1993). Geological thermometer suitable for mantle-derived xenoliths. *Acta Petrol. Sin.*, 167–180. (in Chinese with English abstract).

Yin, C. Q., Qiao, H. Z., Lin, S. F., Li, C. C., Zhang, J., Qian, J. H., et al. (2020). Deformation history of the qianlishan complex, khondalite belt, north China: structures, ages and tectonic implications. *J. Struct. Geol.* 141, 104176. doi:10.1016/j.jsg.2020.104176

Yin, C. Q., Zhao, G., Xiao, W., Lin, S., Gao, R., Zhang, J., et al. (2023). Paleoproterozoic accretion and assembly of the Western Block of North China: a new model. *Earth-Science Rev.* 241, 104448. doi:10.1016/j.earscirev.2023.104448

Yin, C. Q., Zhao, G. C., and Sun, M. (2015). High-pressure pelitic granulites from the helanshan complex in the khondalite belt, north China craton: metamorphic P-T path and tectonic implications. *Am. J. Sci.* 315, 846–879. doi:10.2475/09.2015.03

Yin, C. Q., Zhao, G. C., Sun, M., Xia, X. P., Wei, C. J., Zhou, X. W., et al. (2009). LA-ICP-MS U-Pb zircon ages of the qianlishan complex: constrains on the evolution of the khondalite belt in the western block of the North China craton. *Precambrian Res.* 174, 78–94. doi:10.1016/j.precamres.2009.06.008

Yin, C. Q., Zhao, G. C., Wei, C. J., Sun, M., Guo, J. H., and Zhou, X. W. (2014). Metamorphism and partial melting of high-pressure pelitic granulites from the qianlishan complex: constraints on the tectonic evolution of the khondalite belt in the North China craton. *Precambrian Res.* 242, 172–186. doi:10.1016/j.precamres.2013.12.025

Zhai, M. G. (2010). Tectonic evolution and metallogenesis of north China craton. *Mineral. Deposits* 29, 24–36. (in Chinese with English abstract).

Zhai, M. G. (2022). Khondalite revisited——record of special geological processes on Earth. *Acta Geol. Sin.* 96, 2967–2997. (in Chinese with English abstract).

Zhai, M. G., and Peng, P. (2007). Paleoproterozoic events in the North China craton. *Acta Petrol. Sin.* 23, 2665–2682. (in Chinese with English abstract).

Zhai, M. G., and Santosh, M. (2011). The early Precambrian odyssey of the North China Craton: a synoptic overview. *Gondwana Res.* 20, 6–25. doi:10.1016/j.gr.2011.02.005

Zhai, M. G., and Santosh, M. (2013). Metallogeny of the North China craton: link with secular changes in the evolving earth. *Gondwana Res.* 24, 275–297. doi:10.1016/j.gr.2013.02.007

Zhai, M. G., Zhu, X. Y., Zhou, Y. Y., Zhao, L., and Zhou, L. G. (2020). Continental crustal evolution and synchronous metallogeny through time in the North China Craton. *J. Asian Earth Sci.* 194, 104169. doi:10.1016/j.jseaes.2019.104169

Zhao, G. C. (2009). Metamorphic evolution of major tectonic units in the basement of the North China Craton: key issues and discussion. *Acta Petrol. Sin.* 25, 1772–1792. (in Chinese with English abstract).

Zhao, G. C., Wilde, S. A., Cawood, P. A., and Sun, M. (2001). Archean blocks and their boundaries in the North China Craton: lithological, geochemical, structural and *P–T* path constraints and tectonic evolution. *Precambrian Res.* 107, 45–73. doi:10.1016/s0301-9268(00)00154-6

Zhao, G. C., and Zhai, M. G. (2013). Lithotectonic elements of precambrian basement in the North China craton: review and tectonic implications. *Gondwana Res.* 23, 1207–1240. doi:10.1016/j.gr.2012.08.016

Zhong, C. T., Deng, J. F., Wan, Y. S., Mao, D. B., and Li, H. M. (2007). Magma recording of Paleoproterozoic orogeny in central segment of northern marginof North China Craton: geochemical characteristics and zircon SHRlMP dating of S-type granitoids. *Geochimica*, 585–600.

Zhong, S., Feng, C., Seltmann, R., Li, D., and Qu, H. (2018). Can magmatic zircon be distinguished from hydrothermal zircon by trace element composition? The effect of mineral inclusions on zircon trace element composition. *Lithos* 314-315, 646–657. doi:10.1016/j.lithos.2018.06.029

Zhou, Z. G., Hu, M. M., Wu, C., Wang, G. S., Liu, C. F., Cai, A. R., et al. (2018a). Coupled U-Pb dating and Hf isotopic analysis of detrital zircons from Bayan Obo Group in Inner Mongolia: constraints on the evolution of the Bayan Obo rift belt. *Geol. J.* 53, 2649–2664. doi:10.1002/gj.3102

Zhou, Z. G., Wang, G. S., Di, Y. J., Gu, Y. C., Zhang, D., Zhu, W. P., et al. (2018b). Discovery of mesoproterozoic kimberlite from dorbed banner, inner Mongolia and its tectonic significance. *Geol. J.* 53, 992–1004. doi:10.1002/gj.2939

Zhou, Z. G., Wang, G. S., Zhang, D., Gu, Y. C., Zhu, W. P., Liu, C. F., et al. (2016). Zircon ages of gabbros in the siziwangqi, inner Mongolia and its constrain on the formation time of the bayan Obo group. *Acta Petrol. Sin.* 32, 1809–1822. (in Chinese with English abstract).